

# Charge Collection and Electrical Characterization of Neutron Irradiated Silicon Pad Detectors for the CMS High Granularity Calorimeter

N. Akchurin<sup>a</sup>, P. Almeida<sup>b</sup>, M. Alyari<sup>c</sup>, T. Bergauer<sup>d</sup>, E. Brondolin<sup>b</sup>, Z. Gecse<sup>c</sup>, V. Kuryatkov<sup>e</sup>, R. Lipton<sup>c</sup>, M. Mannelli<sup>b</sup>, T. Mengke<sup>a</sup>, P. Paulitsch<sup>d</sup>, T. Peltola<sup>\*a</sup>, F. Pitters<sup>d</sup>, E. Sicking<sup>b</sup>, M. Vicente Barreto Pinto<sup>b</sup>, Z. Wang<sup>a</sup>, R. Yohay<sup>f</sup>

<sup>a</sup>*Texas Tech University, Department of Physics and Astronomy, Lubbock, TX 79409, USA*

<sup>b</sup>*CERN, 1211 Geneva 23, Switzerland*

<sup>c</sup>*Fermi National Accelerator Laboratory, PO Box 500, Batavia, IL 60510, USA*

<sup>d</sup>*Institut für Hochenergiephysik, 1050 Vienna, Austria*

<sup>e</sup>*Texas Tech University, Nanotech Center, Lubbock, TX 79409, USA*

<sup>f</sup>*Florida State University, Tallahassee, FL 32306, USA*

---

## Abstract

The replacement of the existing endcap calorimeter in the Compact Muon Solenoid (CMS) detector for the high-luminosity LHC (HL-LHC), scheduled for 2027, will be a high granularity calorimeter. It will provide detailed position, energy, and timing information on electromagnetic and hadronic showers in the immense pileup of the HL-LHC. The High Granularity Calorimeter (HGCal) will use 120-, 200-, and 300- $\mu\text{m}$  thick silicon (Si) pad sensors as the main active material and will sustain 1-MeV neutron equivalent fluences up to about  $10^{16} \text{ n}_{\text{eq}}\text{cm}^{-2}$ . In order to address the performance degradation of the Si detectors caused by the intense radiation environment, irradiation campaigns of test diode samples from 8-inch and 6-inch wafers were performed in two reactors. Characterization of the electrical and charge collection properties after irradiation involved both bulk polarities for the three sensor thicknesses. Since the Si sensors will be operated at -30 °C to reduce increasing bulk leakage current with fluence, the charge collection investigation of 30 irradiated samples was carried out with the infrared-TCT setup at -30 °C. TCAD simulation results at the lower fluences are in close agreement with the experimental results and provide predictions of sensor performance for the fluence regions not covered by the experimental study. All investigated sensors display 60% or higher charge collection efficiency at their respective highest lifetime fluences when operated at 800 V, and display above 90% at the lowest fluence, at 600 V. The collected charge close to the fluence of

---

<sup>\*</sup>Corresponding author

*Email address:* [timo.peltola@ttu.edu](mailto:timo.peltola@ttu.edu) (T. Peltola)

$10^{16}$  n<sub>eq</sub>cm<sup>-2</sup> exceeds 1 fC at voltages beyond 800 V.

---

## 1. Introduction

Silicon (Si)-based high granularity technology was chosen for replacement of the existing CMS experiment’s endcap calorimeter for the era of the high-luminosity Large Hadron Collider (HL-LHC) [1]. The HL-LHC is expected to increase the instantaneous luminosity of LHC by at least a factor of five and deliver an estimated integrated luminosity of  $3,000\text{--}4,000\text{ fb}^{-1}$  in 10 years of operation<sup>1</sup>, resulting in maximum integrated doses in excess of 1.5 MGy and neutron fluences of about  $1.0 \times 10^{16} \text{ n}_{\text{eq}}\text{cm}^{-2}$  that the CMS endcap calorimeters must sustain [2].

The High Granularity Calorimeter (HGCAL) aims to perform 3D-position, energy and time measurements in the endcap region ( $1.5 \leq |\eta| \leq 3.2$ ). The electromagnetic calorimeter (CE-E) consists of 28 layers of silicon sensors, with Cu, Cu/W, and Pb absorbers. Similar silicon sensor technology is utilized in the high-radiation region of the hadronic calorimeter (CE-H) for the 8 front layers interleaved with steel absorber plates, while the following 14 layers combine silicon sensors, with plastic scintillator readout by silicon photomultipliers (SiPM) in the higher- and lower- $\eta$  regions, respectively. The approximately 27,000 hexagonal 8-inch silicon modules<sup>2</sup> represent about 6M channels and an area of 600 m<sup>2</sup>. The hexagonal shape of the sensors maximizes the usable area of the circular wafers while remaining tileable. The main properties of the silicon detector channels, along with their expected fluences for the HGCAL, are given in Table 1. The detectors must operate in a high-radiation environment for a decade, while maintaining sufficient signal-to-noise performance for minimum-ionizing particle (MIP) detection. Clean MIP detection in each sensor cell is required to achieve acceptable inter-cell calibration accuracy. Macroscopic radiation damage in the silicon bulk manifests as increase in leakage current, space charge, and trapping of the drifting charge, all of which are detrimental to the performance of a silicon detector [3, 4].

The increase of leakage current with fluence will be mitigated by operating the silicon sensors at -30 °C (243 K). In response to the trapping of the drifting charge, thinner sensors will be used at the higher- $\eta$  (smaller radius) regions of the endcaps, along with high voltage operation ( $\geq 600$  V for heavily-irradiated sensors) and readout at segmented n<sup>+</sup> electrodes collecting electrons (*n*-on-*p* sensors) in all regions. In this study, we discuss experimental and simulation results from the test diodes diced from the full sensor wafers.

The studies of the detector response, which used a sub-nanosecond IR-laser, provide information on

---

<sup>1</sup><https://home.cern/resources/faqs/high-luminosity-lhc>

<sup>2</sup>The prototyping was done with sensors originating from 6-inch wafers, while 8-inch wafers were chosen to reduce the total number of modules needed for the HGCAL.

Table 1: Hexagonal Si sensor cells (DC-coupled planar diodes without biasing structure) in CE-E and CE-H all-silicon layers, showing the properties of different sensor types and the expected 1-MeV equivalent neutron fluence for each type after an estimated integrated luminosity of 3,000–4,000  $\text{fb}^{-1}$ . The upper fluence limits are the current estimates for the highest levels that may be reached, which are somewhat larger than in [2]. The lowest lifetime fluences at the outer radii of each region are roughly equal to the highest fluence of the next region, while in the case of 300- $\mu\text{m}$  thick sensors, it is about  $1 \times 10^{14} \text{ n}_{\text{eq}}\text{cm}^{-2}$ .

Active thickness [ $\mu\text{m}$ ]	300	200	120
Cell size [ $\text{cm}^2$ ]	1.18	1.18	0.52
Cell capacitance [pF]	45	65	50
Highest lifetime fluence ( $\Phi_{\text{max}}$ ) [ $\text{n}_{\text{eq}}\text{cm}^{-2}$ ]	$(5 - 6) \times 10^{14}$	$(2.5 - 3) \times 10^{15}$	$(0.92 - 1) \times 10^{16}$

the carrier transport and electric field distribution in the sensor bulk, which are the input parameters for the long-term prediction of the detector’s charge collection efficiency (CCE) with increasing fluence. By complementing observed CCE with leakage current and capacitance measurements, an extensive picture of the macroscopic effects from the microscopic radiation-induced defects in the silicon bulk is obtained that continue to refine guidelines for detector design and operation.

In a previous study [5] with deep-diffused float-zone (dd-FZ) and epitaxial test diodes at -20 °C, the 300- $\mu\text{m}$ -thick  $n$ -types were found to collect significantly more charge than the  $p$ -type sensors at a fluence of  $5 \times 10^{14} \text{ n}_{\text{eq}}\text{cm}^{-2}$ , while negligible differences in charge collection between the two sensor types were observed for thinner sensors at their respective expected maximum fluences. Additionally, epitaxial 100- $\mu\text{m}$  active thickness diodes were reported to display substantially better charge collection performance compared to the 120- $\mu\text{m}$  dd-FZ diodes at the fluence of  $1.0 \times 10^{16} \text{ n}_{\text{eq}}\text{cm}^{-2}$ . The following results complete the study introduced in [6] and address the processes leading to the observations described above. The study involved 30 irradiated test diode samples diced from 8-inch (shallow diffused-FZ and epitaxial) and 6-inch (standard and deep diffused-FZ) wafers.

The experimental results were reproduced with Technology Computer-Aided Design (TCAD) simulations that allow reconstruction of the potential and electric field distributions as well as the charge and current response of the irradiated test diodes within the validated fluence range of the defect model for neutrons [7, 8]. In the light of an earlier charge collection study at extreme fluences [9], the investigation of 200- and 300- $\mu\text{m}$ -thick  $n$ -on- $p$  sensors is extended beyond their respective maximum lifetime fluences up to about

$1 \times 10^{16} \text{ n}_{\text{eq}}\text{cm}^{-2}$ . The CCE evolution of the two sensor thicknesses is presented.

The radiation hardness results presented here cover only the bulk properties of the silicon sensor. Investigations of surface properties for the functionality of a multi-channel detector –such as of accumulation of Si/SiO<sub>2</sub> interface charge density with fluence, charge sharing, and inter-electrode capacitances and resistances– are presently ongoing.

The paper is arranged in following order: Section 2 introduces the samples and target fluences involved in the neutron irradiation campaign. Measurement and simulation setups are presented in Section 3. In Section 4, characterization results of irradiated pad sensors are presented by first extracting effective fluences ( $\Phi_{\text{eff}}$ ) from the leakage current volume density. Next, measured and simulated charge collection results are presented, followed by full depletion voltages ( $V_{\text{fd}}$ ) extracted from the capacitance-voltage data. Finally, the results are discussed and summarised in Sections 5 and 6.

## 2. Neutron irradiation campaign

### 2.1. Samples and target fluences

The irradiation campaigns were carried out in reactors in two facilities, Rhode Island Nuclear Science Center<sup>3</sup> (RINSC) and UC Davis McClellan Nuclear Research Center<sup>4</sup> (MNRC). The two independent irradiation runs, 16 samples at RINSC and 14 samples at MNRC, were included in the study in order to cross-check dosimetry of the facilities as well as the method by which the effective fluences are extracted from the leakage current ( $I_{\text{leak}}$ ) of the samples after the irradiation.

Samples in Figures 1 and 2 were diced from 8-inch and 6-inch Hamamatsu Photonics K.K. (HPK) sensors. Since the deep diffusion process used by HPK for reducing the active thickness to 300, 200, and 120  $\mu\text{m}$ , while maintaining the physical thickness to 320  $\mu\text{m}$ , was only applied to the 6-inch wafers, the 8-inch 200- and 300- $\mu\text{m}$ -thick sensors have the same physical and active thickness. Three distinct diffusion processes were applied to produce the heavily-doped backplane blocking contact: in 6-inch wafers standard-diffusion ('std-FZ') to produce 300- $\mu\text{m}$  active thickness sensors and deep-diffusion ('dd-FZ') for 200- and 120- $\mu\text{m}$  active thickness, while the 8-inch wafers applied shallow-diffusion ('shd-FZ') for 300- and 200- $\mu\text{m}$ -thick sensors. The only 8-inch wafer sensor in the study with a nominal active thickness of 120  $\mu\text{m}$  was produced by growing epitaxial silicon on a lower resistivity substrate, resulting in a total physical thickness of 300

---

<sup>3</sup><http://www.rinsc.ri.gov/>

<sup>4</sup><https://mnrc.ucdavis.edu/>

$\mu\text{m}$  [2]. While the substrate material of both 6- and 8-inch wafers is float-zone Si, the 8-inch wafers have roughly an-order-of-magnitude lower oxygen concentration in the bulk relative to the 6-inch wafers. All the samples in the irradiation campaign are listed in Table 2. The samples are identified in Section 4 by e.g. ‘shd-FZ\\_LO\\_300P’ that refers to a 300- $\mu\text{m}$ -active thickness float-zone *n*-on-*p* type sensor with shallow diffused backplane implant and low oxygen bulk concentration (all varieties are presented in Table 2).

The 16 samples irradiated at the RINSC reactor were exposed at all six fluence levels shown in Table 2. The facility’s dosimetry is based on the activation data of ultrapure foils of several different elements. Neutron flux spectrum of the reactor is extracted by using the known cross section of these elements to interact with neutrons as a function of energy. This measured neutron flux spectrum is then convoluted with the damage function for silicon [10] and integrated to obtain the 1-MeV neutron equivalent flux of  $\phi = (4.0 \pm 0.8) \times 10^{11} \text{ cm}^{-2}\text{s}^{-1}$ . Since this method assumes a fixed neutron flux spectrum, the dominant uncertainty is related to the contribution from thermal neutrons. For the six irradiation times ranging from 5.8 min to 383.2 min, this method resulted in about 20% uncertainty in the dosimetry determined fluences.

The 14 samples irradiated at the MNRC reactor were exposed to the four highest fluences listed in Table 2. The first fluence was measured to be  $7.37 \times 10^{14} \text{ n}_{\text{eq}}\text{cm}^{-2}$  using the fast sulfur activation method. The errors associated with this method are counting uncertainty in measuring the activation of  $^{32}\text{P}$  ( $< 0.5\%$ ), and the small non-uniformity in the flux along the length of the samples which contributes at most 5%. Since higher fluences would have made the sulfur samples too radioactive, the other three fluences were estimated based on the dosimetry results from the first irradiation. The reactor power levels were increased linearly to reach the higher fluences, resulting in a maximum uncertainty of 5% associated with the sample position, with additional 5% uncertainty associated with the normal power fluctuations in the reactor. When the uncertainties were assumed to be independent, the maximum dosimetry uncertainty expected for the three higher power irradiations was at most 7%.

The dosimetry-determined fluences from both irradiation facilities, along with the target fluences and the leakage current extracted effective fluences, are further discussed in Section 4.1.

After irradiation, the samples were shipped in thermally isolated containers packed with cold gel to Texas Tech University (TTU) to avoid annealing of the radiation induced defects, and were then kept at -40 °C at all times between the measurements.

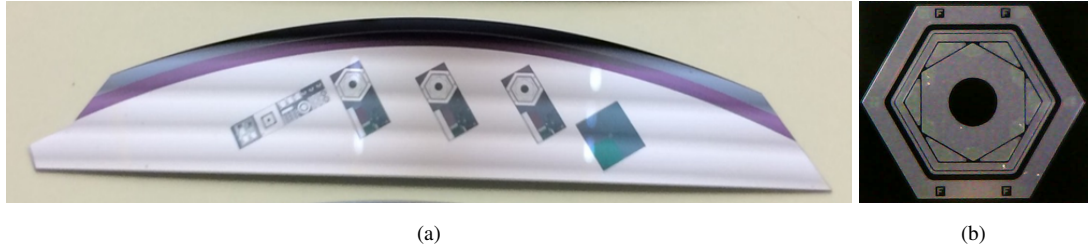


Figure 1: (a) Half moon sample with three test diodes and other test structures diced from an 8-inch Si wafer. (b) Close-up of the hexagonal test diode on the half moon sample. Tip to tip, the outer ring measures 4.5 mm.

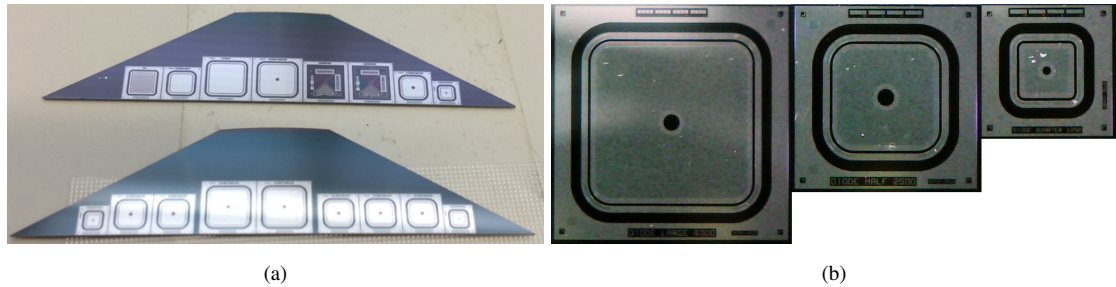


Figure 2: (a) Half moon samples with test structures diced from a 6-inch Si wafer. Top: three test diodes, MOS- and other test structures. Bottom: nine test diodes. (b) Close-up of the three square diode sizes ( $4.0 \times 4.0 \text{ mm}^2$ ,  $2.5 \times 2.5 \text{ mm}^2$ ,  $1.25 \times 1.25 \text{ mm}^2$ ) with laser entrance windows in the center.

Table 2: Target fluences and irradiated samples. Bulk material is indicated as ‘shd-’, ‘std-’ and ‘dd-FZ’ that correspond to shallow-, standard- and deep-diffused float zone, respectively, and ‘epi’ for epitaxial. High and low oxygen bulk concentrations are indicated as ‘HO’ and ‘LO’, respectively. The two values in each entry in columns 3–8 indicate the number of samples irradiated at RINSC and MNRC reactors, respectively. The ‘wafer size’ refers to the size of the full wafers from which the test samples were diced off.

Wafer size	Sensor type & thickness	Target fluence [ $\text{n}_{\text{eq}}\text{cm}^{-2}$ ]					
		$1.5 \times 10^{14}$	$5.0 \times 10^{14}$	$7.5 \times 10^{14}$	$1.5 \times 10^{15}$	$3.8 \times 10^{15}$	$1.0 \times 10^{16}$
8"	shd-FZ\_LO\_300P	1 + 0	1 + 0	2 + 2			0 + 1
	shd-FZ\_LO\_200P				1 + 0	1 + 1	0 + 1
	epi\_LO\_120P					0 + 1	
6"	std-FZ\_HO\_300P				0 + 1	0 + 1	0 + 1
	dd-FZ\_HO\_120P				1 + 0	1 + 0	1 + 2
	std-FZ\_HO\_300N	1 + 0	1 + 0	1 + 1			
	dd-FZ\_HO\_200N				1 + 0		
	dd-FZ\_HO\_120N					2 + 0	1 + 2

### 3. Measurement and simulation setups

#### 3.1. CV/IV-probestation

For the capacitance-voltage/current-voltage (CV/IV) characterization, a custom probe station has been constructed at TTU that provides cooling to about -10 °C in a dry environment and bias voltages up to 2.0 kV for the measurements of heavily-irradiated Si sensors. The bias voltage is supplied by a Keithley 2410 SourceMeter (SMU) up to 1.1 kV (or two back-to-back connected SMUs up to 2.0 kV) while the leakage current and capacitance are read out by a Keithley 6485 Picoammeter and a HP4274A LCR-meter, respectively. The DC-separation up to 2.0 kV of the LCR-meter’s high- and low-terminals is accomplished by 1- $\mu\text{F}$  capacitors. The remote control and data acquisition functions are carried out with LabVIEW<sup>TM</sup>-based software.

The test diode is connected to the measurement circuit by a vacuum chuck from its backplane, which also provides fixed position, and by probe needles on the segmented front surface for the diode region and guard-ring, respectively. A Peltier cooler below the stainless-steel chuck provides cooling while the heat from the

Peltier is removed by a closed circuit liquid cooling system. The sample temperature and the humidity inside the cooling box are monitored by a thermocouple and a Vaisala DSS70A dew point meter, respectively.

Since full depletion voltage ( $V_{fd}$ ) has negligible sensitivity to measurement temperature in the studied  $T$ -range, the  $CV$ -measurements were carried out below  $+5$  °C to suppress leakage current to  $\leq 1$  mA during  $V$ -ramping for low power dissipation. Due to high sensitivity of leakage current to the measurement temperature, the temperature during  $IV$ -measurements was fixed as closely as possible to  $+5$  °C.

### 3.2. TCT-setup

The infrared-Transient Current Technique (IR-TCT) setup constructed at TTU for the measurement campaign is based on a Particulars commercial system<sup>5</sup> and modified to accommodate the investigated samples from 8-inch and 6-inch wafers at  $-30$  °C. The setup includes an IR-pulse generator of  $1.06$  μm wavelength that is connected by an optical fiber to a beam expander, which was placed about 85 mm above the center of the investigated diode that was mounted on an  $xy$ -translation stage. The diode was biased at the front side with a Keithley 2410 SMU and read out through a Bias-T with a 53 dB amplifier and a 2.5 GHz Tektronix DPO 7254 oscilloscope with 10 GS/s and  $50\ \Omega$  termination. The remote control and DAQ of the circuit components are provided by LabVIEW™-based software.

The IR-TCT setup produces well-defined and stable transient signals that can be closely reproduced by simulation, as shown in Figure 3 (simulation parameters are introduced in Section 3.3). The IR-laser mimics a MIP by penetrating the entire thickness of the silicon sensors, thus providing straightforward means for a CCE investigation. A wire-bond connection minimizing the signal path between the sensor and the SMA cable was found to be essential in minimizing signal undershoot and reflections.

The setup utilizes four Peltier coolers to achieve  $-30$  °C sample temperature. As in the  $CV/IV$ -setup, to avoid any condensation,  $N_2$  flow was supplied to the sample during cooling. The temperature and humidity monitoring are accomplished by a four-wire resistance temperature detector (RTD) circuit and a Vaisala DSS70A dew point meter, respectively, thus ensuring that all measurements were carried out above dew point temperature.

---

<sup>5</sup><http://www.particulars.si>

### 3.3. Simulation setup and parameters

All simulations in this paper were carried out using the Synopsys Sentaurus<sup>TM</sup><sup>6</sup> finite-element TCAD software framework. The simulations applied Neumann boundary conditions as well as Dirichlet boundary conditions for carrier densities and AC potential at Ohmic contacts that were used to excite the system.

For the simulation of the evolution of electrical properties and charge collection with fluence, the two dimensional structures presented in Figure 4 were applied. The sensor width was set to wide enough to fully contain the generated charge carrier clouds within the structure during the transient simulation, when the laser illumination was performed at the center of the front surface ( $x = 100, y = 0$  in Figure 4a). The simulation was focused at the center part of the test diodes. Due to the large surface areas of the real diodes, any contribution from the edges to the local electric fields at the center were considered negligible, and no edge regions were included in the modeled structures.

The parameters extracted from *CV/IV*- and TCT-measurements before irradiation (bulk doping, active thickness, charge carrier trapping times, and backplane doping profiles for deep-diffused diodes) were used as an input to reproduce the devices as closely as possible by simulation. Doping profiles of all modeled diodes are presented in Figure 4b.

All modeled sensors were DC-coupled (with no oxide layer between the collecting electrode and Si bulk) as the real devices. High potential was provided from the backplane contact, while the front surface electrode at zero potential was used for charge collection in transient simulations.

As in the experimental setup, an IR-laser of 1.06  $\mu\text{m}$  wavelength and sufficient penetration depth to model a MIP was applied to generate charge carriers in the detector. The laser spot diameter was set to 11  $\mu\text{m}$  and the pulse length to 0.45 ns to match the values used in the IR-TCT setup. The laser intensity was tuned to produce MIP equivalent collected charge (22  $\text{ke}^-$  in 300  $\mu\text{m}$  of silicon), while generating low enough  $e-h$  pair density (about 1100  $\mu\text{m}^{-2}$ ) to avoid any space charge density current effects that might modify sensor properties during the transient simulation. The bias-T circuit was modeled by including a high-resistance bias circuit and a charge-collection circuit with 50  $\Omega$  termination to the DC- and AC-parts of the simulation, respectively.

In heavily-irradiated silicon sensors (between  $10^{14}$  to  $10^{16}$   $\text{n}_{\text{eq}}\text{cm}^{-2}$ ), carrier trapping is the main factor reducing the collected charge. To model this in simulation, a neutron defect model [7], validated from  $1 \times 10^{14}$   $\text{n}_{\text{eq}}\text{cm}^{-2}$  up to  $1 \times 10^{15}$   $\text{n}_{\text{eq}}\text{cm}^{-2}$  and presented in Table 3, was applied. The neutron defect model

---

<sup>6</sup><http://www.synopsys.com>

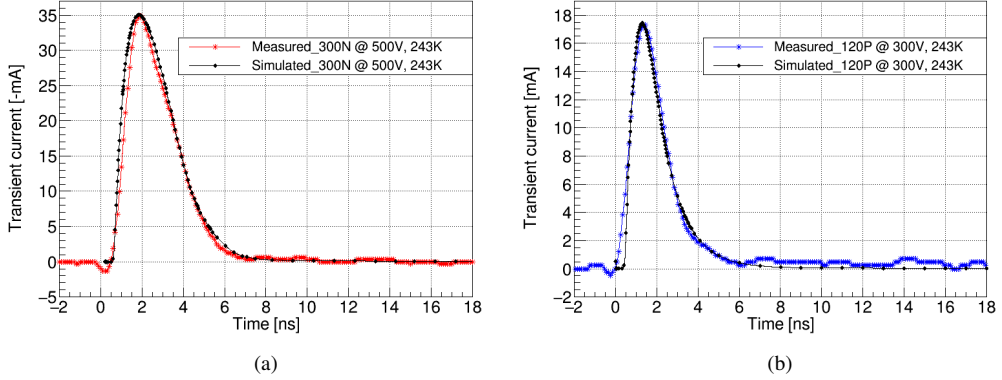


Figure 3: Examples of measured and simulated transient signals for (a) 300N and (b) dd-FZ 120P sensors. Both the measurements and the simulations were carried out with a 11  $\mu\text{m}$  wide IR-laser spot, matching bias voltages and at -30  $^{\circ}\text{C}$ . The sensor parameters used in the simulation were extracted from  $CV/IV$ -measurements.

Table 3: The parameters of the neutron defect model for Synopsys Sentaurus<sup>TM</sup>TCAD [7].  $E_{\text{c},\text{v}}$  are the conduction band and valence band energies,  $\sigma_{\text{e},\text{h}}$  are the electron and hole trapping cross sections, and  $\Phi$  is the 1-MeV neutron equivalent fluence.

Defect type	Level [eV]	$\sigma_{\text{e},\text{h}} [\text{cm}^2]$	Concentration [ $\text{cm}^{-3}$ ]
Deep acceptor	$E_{\text{c}} - 0.525$	$1.2 \times 10^{-14}$	$1.55 \times \Phi$
Deep donor	$E_{\text{v}} + 0.48$	$1.2 \times 10^{-14}$	$1.395 \times \Phi$

was chosen over other models for higher fluences (e.g. [11]) because, at the moment, it is the only model that has been shown to closely reproduce the experimentally observed evolution with fluence of leakage current, full depletion voltage, and double-peak electric field distribution in the Si bulk, as well as charge collection efficiency. Although the model still reproduces expected leakage current well beyond the  $1 \times 10^{15} \text{ n}_{\text{eq}}\text{cm}^{-2}$  limit over which it has been validated, the effective bulk doping ( $N_{\text{eff}}$ ) increase with fluence becomes exaggerated, leading to high enough electric fields to generate  $e-h$  avalanche that in turn leads to CCE values not in line with experimental observations. All charge collection simulations were carried out at matching temperature ( $T = 243 \text{ K}$ ) to the measurements.

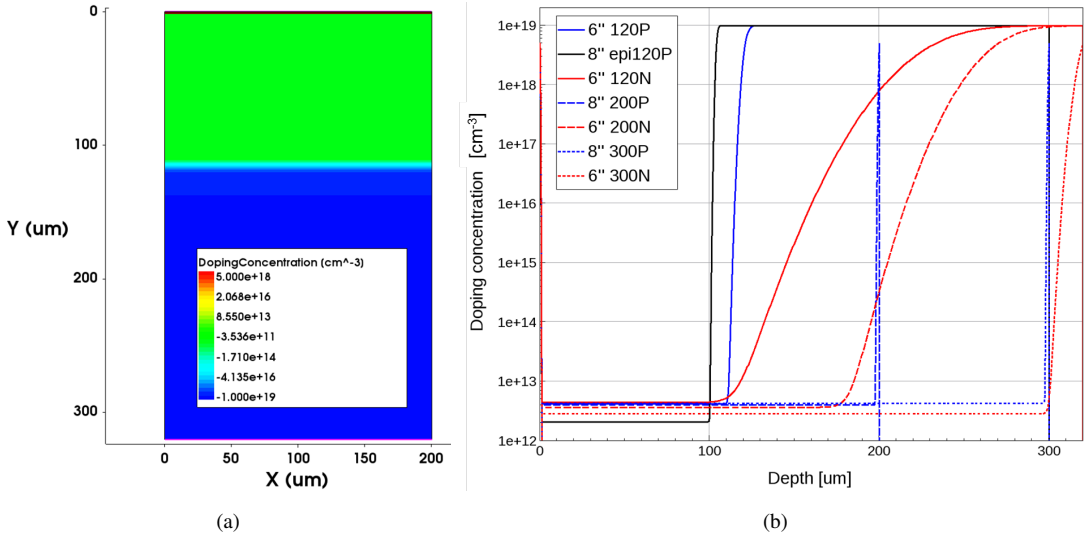


Figure 4: Modeled sensor structures and doping profiles before irradiation. (a) A two dimensional  $n$ -on- $p$  sensor structure with 200  $\mu\text{m}$  width, 320  $\mu\text{m}$  physical thickness, and deep-diffusion thinned active thickness of 111  $\mu\text{m}$ . (b) Doping profiles of all simulated sensor structures. The crystal orientation of the bulk material was set to  $\langle 1, 0, 0 \rangle$ .

#### 4. Characterization after irradiation

##### 4.1. Leakage currents and effective fluences

The leakage current ( $I_{\text{leak}}$ ) measurements of the irradiated samples were carried out at +5 °C up to a voltage of 1.1 kV. The  $I_{\text{leak}}$  of fully depleted diodes, monitored by  $CV$ -measurements and discussed further in Section 4.3, was then used to determine the leakage current volume densities. For the active volumes, the diode area ( $A$ ) information shown in Figures 1 and 2 was used in combination with active thicknesses ( $d$ ) extracted from measured geometrical capacitances ( $C_{\text{geom}} = \epsilon_0 \epsilon_s A/d$ , where  $\epsilon_0$  and  $\epsilon_s$  are the vacuum permittivity and the relative permittivity of silicon, respectively [12]).

Since current-related damage rate  $\alpha$  has been shown to be strictly proportional to the 1-MeV neutron equivalent fluence as well as being independent of the silicon material, it is defined by [13]

$$\frac{\Delta I_{\text{leak}}}{V} = \alpha \Phi_{\text{eff}}, \quad (1)$$

where  $\Delta I_{\text{leak}}$  is the change in the leakage current due to irradiation,  $V$  is the active volume of either  $p$ - or  $n$ -type detector, and  $\Phi_{\text{eff}}$  is the 1-MeV neutron equivalent effective fluence. By using Eq. 1, the  $\Delta I_{\text{leak}}/V$

extracted  $\Phi_{\text{eff}}$  was determined by using  $\alpha(293 \text{ K}) = 4.0 \times 10^{-17} \text{ A/cm}$ , a value established in previous studies [13, 14]. To scale the  $+5 \text{ }^{\circ}\text{C}$  measured leakage currents to room temperature, a method described in [15] was applied. Several diodes were measured, and the final  $\Phi_{\text{eff}}$  was determined as the mean value for all the samples corresponding to a given target fluence at a respective irradiation facility, as shown in Table 2.

The results, along with the fluences determined by the dosimetry of the two irradiation facilities, are presented in Table 4. When  $\Phi_{\text{dosi}}$  values and  $\alpha(293 \text{ K})$  are inserted into Eq. 1, the resulting expected mean  $\alpha$ -values for RINSC and MNRC are  $(4.3 \pm 2.0) \times 10^{-17} \text{ A/cm}$  and  $(4.0 \pm 0.7) \times 10^{-17} \text{ A/cm}$ , respectively, when extracted from calculated leakage current volume density as a function of  $\Phi_{\text{dosi}}$ . Corresponding  $\alpha$ -values extracted from the measured leakage current volume density as a function of  $\Phi_{\text{dosi}}$  yield for RINSC and MNRC  $(3.2 \pm 1.1) \times 10^{-17} \text{ A/cm}$  and  $(3.9 \pm 0.9) \times 10^{-17} \text{ A/cm}$ , respectively. Alternatively, when  $\Phi_{\text{eff}}$  is plotted as a function of  $\Phi_{\text{dosi}}$ , the resulting slopes for RINSC and MNRC are  $0.8 \pm 0.3$  and  $1.0 \pm 0.2$ , respectively, displaying agreement within uncertainty between data sets.

All the measurements in this and the following sections were taken after about 10 min at  $60 \text{ }^{\circ}\text{C}$ , which is identical to the approach described in a previous Si sensor radiation hardness study for HGCAL [5]. Additionally, after all samples had been TCT- and *CV*-characterized, five samples exposed to four different fluences were annealed 80 min at  $60 \text{ }^{\circ}\text{C}$  and *IV*-measured again. The resulting  $\alpha(293 \text{ K})$ -factors extracted before and after the 80 min annealing for the four fluence points were  $(3.83 \pm 0.74) \times 10^{-17} \text{ A/cm}$  and  $(3.79 \pm 1.12) \times 10^{-17} \text{ A/cm}$ , respectively. Thus, the original *IV*-extracted values were considered to provide a fair estimate of  $\Phi_{\text{eff}}$  and are applied in fluence evolution plots of CCE and  $V_{\text{fd}}$  in the following sections.

## 4.2. Charge collection

### 4.2.1. Extracting CCE from IR-TCT data

To extract the CCE of the irradiated diodes, the IR-laser induced transient currents were first recorded at  $-30 \text{ }^{\circ}\text{C}$  for both the irradiated and non-irradiated-reference samples. This was done to compensate for the observed temperature dependence of the transient-signal amplitudes. The reference and the corresponding irradiated sample were always diced from the same Si wafer to minimize any effect from possible processing differences between the wafers.

Transient currents of the reference diodes were recorded for reverse bias voltages from about 50 V above  $V_{\text{fd}}$  up to 500 V. The laser spot was focused at the center of the laser window (see Figures 1 and 2) and the light intensity was set as low as possible, while not compromising the stability of the transient signal, to avoid

Table 4: Target fluences, dosimetry fluences ( $\Phi_{\text{dosi}}$ ) provided by the irradiation facilities, and *IV*-extracted effective fluences ( $\Phi_{\text{eff}}$ ). All fluences are given in 1-MeV neutron equivalent units.

Facility	Target $\Phi$ [ $\text{n}_{\text{eq}}\text{cm}^{-2}$ ]	$\Phi_{\text{dosi}}$ [ $\text{n}_{\text{eq}}\text{cm}^{-2}$ ]	$\Phi_{\text{eff}}$ [ $\text{n}_{\text{eq}}\text{cm}^{-2}$ ]
RINSC	$1.5 \times 10^{14}$	$(1.5 \pm 0.3) \times 10^{14}$	$(1.05 \pm 0.05) \times 10^{14}$
	$5.0 \times 10^{14}$	$(4.6 \pm 0.9) \times 10^{14}$	$(3.5 \pm 0.4) \times 10^{14}$
	$7.5 \times 10^{14}$	$(7.1 \pm 1.6) \times 10^{14}$	$(5.4 \pm 0.4) \times 10^{14}$
	$1.5 \times 10^{15}$	$(1.3 \pm 0.3) \times 10^{15}$	$(1.5 \pm 0.3) \times 10^{15}$
	$3.8 \times 10^{15}$	$(3.4 \pm 0.7) \times 10^{15}$	$(2.35 \pm 0.19) \times 10^{15}$
	$1.0 \times 10^{16}$	$(8.4 \pm 1.8) \times 10^{15}$	$(6.6 \pm 0.7) \times 10^{15}$
MNRC	$7.5 \times 10^{14}$	$(7.4 \pm 0.4) \times 10^{14}$	$(6.1 \pm 0.5) \times 10^{14}$
	$1.5 \times 10^{15}$	$(1.47 \pm 0.11) \times 10^{15}$	$(1.3 \pm 0.3) \times 10^{15}$
	$3.8 \times 10^{15}$	$(3.7 \pm 0.3) \times 10^{15}$	$(3.47 \pm 0.16) \times 10^{15}$
	$1.0 \times 10^{16}$	$(9.8 \pm 0.7) \times 10^{15}$	$(9.3 \pm 1.1) \times 10^{15}$

any space charge density current effects as well as amplifier saturation. The collected charge ( $Q_{\text{coll}}$ ) was then extracted by integrating the current signal over time. The most probable value of  $Q_{\text{coll}}$  in a fully depleted reference diode was computed as an average of collected charges recorded over all voltages.

28 irradiated samples were included in the CCE study. The investigated voltages for the irradiated samples ranged from 400 V to 1 kV and the same analysis methods described above for reference diodes were applied. The charge collection efficiency was then determined as a ratio  $\text{CCE} = Q_{\text{coll}}(\text{irradiated})/Q_{\text{coll}}(\text{reference})$ . The RTD-monitored mean temperature throughout all measurements was  $T = (-30.10 \pm 0.13) \text{ }^{\circ}\text{C}$ . The CCE results were also converted to the collected charge by considering a MIP-induced charge deposition of 73  $e^-/\mu\text{m}$  in silicon [16]. Both are presented in the following section.

#### 4.2.2. CCE results

##### 300- $\mu\text{m}$ -thick sensors

In Figure 5, the measured results for 300- $\mu\text{m}$  thick diodes also include comparison with TCAD simulated CCE. All expected lifetime fluences for 300- $\mu\text{m}$  thick sensors at HGCAL, from  $1 \times 10^{14} \text{ n}_{\text{eq}}\text{cm}^{-2}$  to about  $(5 - 6) \times 10^{14} \text{ n}_{\text{eq}}\text{cm}^{-2}$  [2], are within the validated range of the neutron defect model. The simulation closely reproduces both voltage (with input fluences within uncertainty of  $\Phi_{\text{eff}}$ , as shown in Table 5) and

Table 5: Sensor identification, *IV*-extracted effective fluences ( $\Phi_{\text{eff}}$ ) and simulation input fluences ( $\Phi_{\text{TCAD}}$ ) for the CCE results in Figure 5a. Bulk material is indicated as ‘shd-’ and ‘std-FZ’ for shallow- and standard-diffused float zone, respectively. High (‘HO’) and low (‘LO’) oxygen bulk concentrations correspond to samples diced from 6- and 8-inch wafers, respectively.

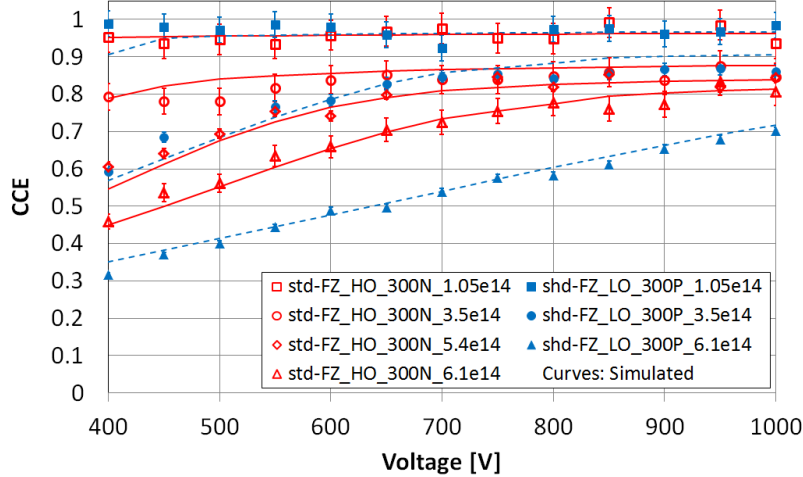
Sensor thickness & type	$\Phi_{\text{eff}}$ [ $n_{\text{eq}}\text{cm}^{-2}$ ]	$\Phi_{\text{TCAD}}$ [ $n_{\text{eq}}\text{cm}^{-2}$ ]
shd-FZ_LO_300P	$(1.05 \pm 0.05) \times 10^{14}$	$1.1 \times 10^{14}$
std-FZ_HO_300N	$(1.05 \pm 0.05) \times 10^{14}$	$1.1 \times 10^{14}$
shd-FZ_LO_300P	$(3.5 \pm 0.4) \times 10^{14}$	$3.2 \times 10^{14}$
std-FZ_HO_300N	$(3.5 \pm 0.4) \times 10^{14}$	$3.9 \times 10^{14}$
std-FZ_HO_300N	$(5.4 \pm 0.4) \times 10^{14}$	$5.2 \times 10^{14}$
std-FZ_HO_300N	$(6.1 \pm 0.5) \times 10^{14}$	$6.0 \times 10^{14}$
shd-FZ_LO_300P	$(6.1 \pm 0.5) \times 10^{14}$	$6.2 \times 10^{14}$

fluence dependence of the measured CCE.

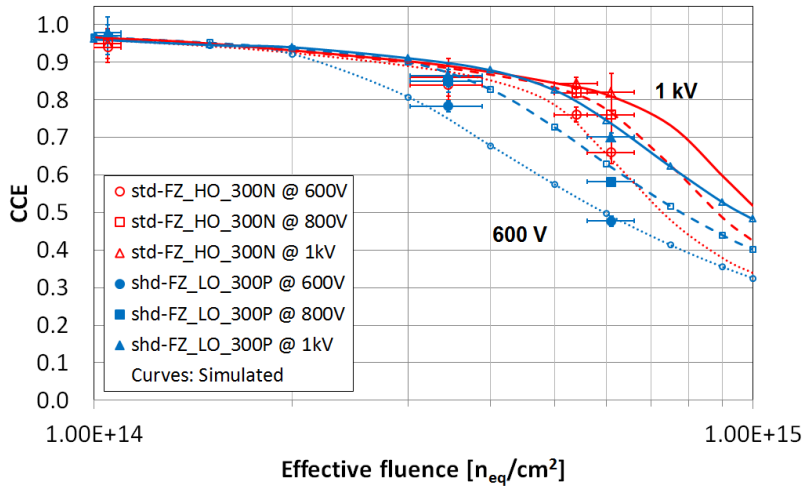
Figure 5b displays significantly better CCE performance for 300N (300- $\mu\text{m}$  thick *p*-on-*n*) sensors compared to 300P above fluence of about  $4 \times 10^{14} \text{ n}_{\text{eq}}\text{cm}^{-2}$ . This is due to space charge sign inversion (SCSI) of the *n*-type substrate that results in the *p*-on-*n* sensor being fully depleted at lower voltages than the *n*-on-*p* in the fluence range of 300  $\mu\text{m}$  thick sensors. At fluences around  $6 \times 10^{14} \text{ n}_{\text{eq}}\text{cm}^{-2}$ , the CCEs of both polarity sensors exhibit 0.1 (10%) and about 0.2 (20%) gains from increasing the operating voltage from 600 V to 800 V and 1 kV, respectively.

#### 200- $\mu\text{m}$ -thick sensors

The results for 200- $\mu\text{m}$ -thick sensors (Figure 6a) show voltage dependence of CCE for the three irradiated samples, which indicates that the sensors are not fully depleted below 800 V, as further discussed in Section 4.3. Because the lifetime fluences of 200- $\mu\text{m}$ -thick sensors are expected to be in the range of  $(0.5 - 2.5) \times 10^{15} \text{ n}_{\text{eq}}\text{cm}^{-2}$  [2], the TCAD simulations in Figure 6b are only applied to the lower part of the fluence range, up to  $1 \times 10^{15} \text{ n}_{\text{eq}}\text{cm}^{-2}$ . Since the lowest target fluence for the irradiated samples was  $1.5 \times 10^{15} \text{ n}_{\text{eq}}\text{cm}^{-2}$ , the simulations provide a complementary view of the CCE behavior throughout the expected fluence range when combined with data points of the 200P sensors. Since only one 200N sam-



(a)



(b)

Figure 5: Evolution of CCE at lowest-fluence region with voltage and fluence for 300- $\mu\text{m}$  thick sensors at -30 °C. Sensor identification is indicated in the legends, as well as effective fluences (in units of  $\text{n}_{\text{eq}}\text{cm}^{-2}$ ) in panel (a). CCE = 1 corresponds to the MIP-induced charge of 22  $\text{ke}^-$  [16]. (a) Measured and simulated (solid and dashed curves for  $p$ -on- $n$  and  $n$ -on- $p$ , respectively, with  $IV$ -extracted effective fluences used as simulation input shown in Table 5) CCE( $V$ ). (b) Measured and simulated (dotted for 600 V, dashed for 800 V and solid curves for 1 kV, with markers on  $n$ -on- $p$  curves) CCE( $\Phi_{\text{eff}}$ ).

ple was available for irradiation, the combined measured and simulated CCE(200N) results go up to about  $1.5 \times 10^{15} \text{ n}_{\text{eq}}\text{cm}^{-2}$ .

The CCE of 200P sensors does better by about 11% and 25% at 800 V and 1 kV, respectively, compared to at 600 V, close to the maximum expected fluence ( $\Phi_{\text{max}}$ ) to which the 200- $\mu\text{m}$  thick sensors will be exposed. Furthermore, at a fluence beyond  $\Phi_{\text{max}}$ , at about  $3.5 \times 10^{15} \text{ n}_{\text{eq}}\text{cm}^{-2}$ , corresponding gains of 16% and 35% are observed.

When extrapolated, the simulated CCE for the 200N sensor is consistent with the measured data points for the three voltages in Figure 6b. About 9% and 12% gains in CCE from increasing the voltage to 800 V and 1 kV, respectively, are observed at the fluence of  $(1.5 \pm 0.3) \times 10^{15} \text{ n}_{\text{eq}}\text{cm}^{-2}$ .

#### *120- $\mu\text{m}$ -thick sensors*

Since the 120- $\mu\text{m}$ -thick sensors will have to operate in a neutron fluence range from about  $2.5 \times 10^{15} \text{ n}_{\text{eq}}\text{cm}^{-2}$  to  $1 \times 10^{16} \text{ n}_{\text{eq}}\text{cm}^{-2}$ , which is well beyond the validated fluence limit of the TCAD neutron defect model, all the curves in Figure 7 are fits to data points.

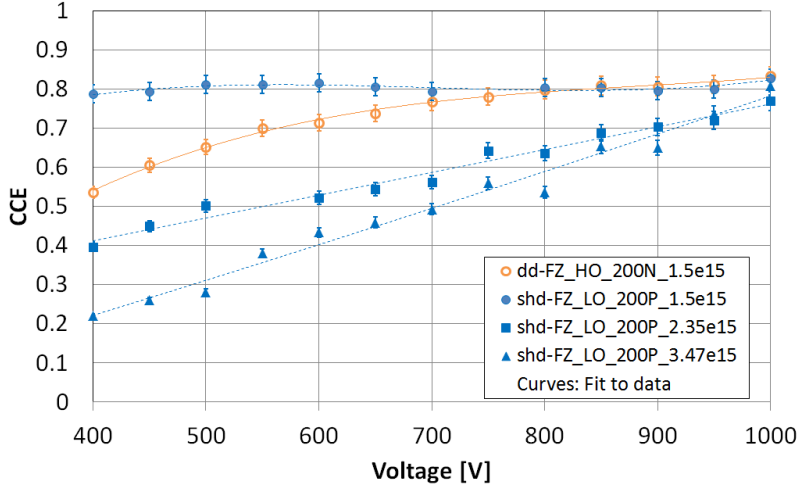
In Figure 7a, the results from the 8-inch epitaxial 120P sample at the fluence of about  $3.5 \times 10^{15} \text{ n}_{\text{eq}}\text{cm}^{-2}$  display higher CCE values than the three lower-fluence data sets from the dd-FZ samples. This could be an indication of charge multiplication produced by high electric fields resulting from radiation induced increase in effective bulk doping ( $N_{\text{eff}}$ ) and needs to be investigated in future studies.

In Figure 7b, the CCEs of both polarity sensors benefit about 20% and 40% due to increased operating voltage from 600 V to 800 V and 1 kV, respectively, at the highest fluence. Both polarities display similar CCE performance at the highest fluences.

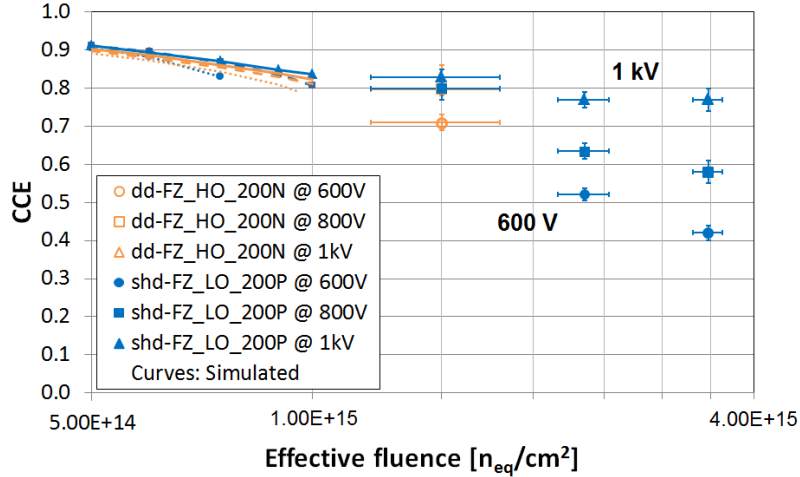
#### *Charge collection summary*

The measured CCE results for the three sensor thicknesses for the full expected fluence range are shown in Figures 8a, 9a, and 10a, while separating for the operating voltages of 600 V, 800 V, and 1 kV, respectively. At fluences around  $\Phi_{\text{max}}$  CCE  $\geq 60\%$  and over 70% are observed at 800 V and 1 kV, respectively, for all measured sensors, while the same level of CCE performance at corresponding fluences is only seen for 300N sensors operated at 600 V, as marked in Figure 8a. Close to lower lifetime fluence limits expected at the outer radii of each sensor thickness ( $1 \times 10^{14} \text{ n}_{\text{eq}}\text{cm}^{-2}$  for 300  $\mu\text{m}$ ,  $5 \times 10^{14} \text{ n}_{\text{eq}}\text{cm}^{-2}$  for 200  $\mu\text{m}$  and  $2.5 \times 10^{15} \text{ n}_{\text{eq}}\text{cm}^{-2}$  for 120  $\mu\text{m}$ ), operating at 600 V provides high CCE performance.

The corresponding MIP-induced charge deposition results in Figures 8b, 9b, and 10b indicate that the

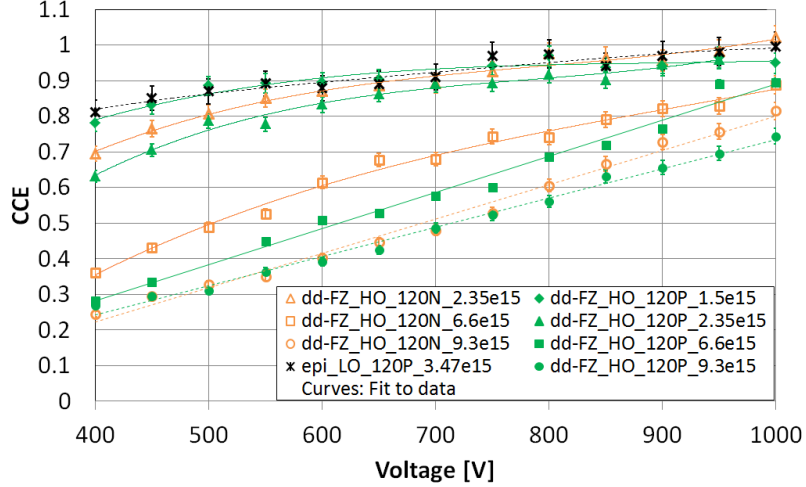


(a)

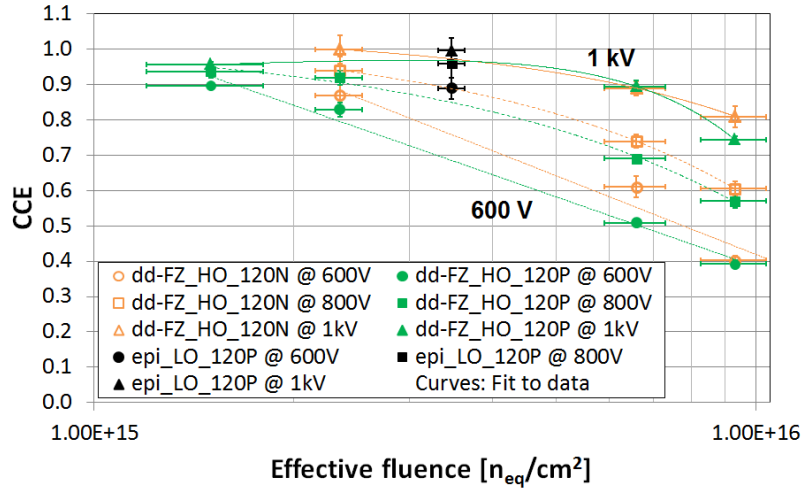


(b)

Figure 6: CCE at intermediate-fluence region as a function of voltage and fluence for 200- $\mu\text{m}$  thick sensors at -30 °C. Sensor identification is indicated in the legends, as well as effective fluences (in units of  $n_{\text{eq}}\text{cm}^{-2}$ ) in panel (a). CCE = 1 corresponds to the MIP-induced charge of 15  $\text{ke}^-$  [16]. (a) Measured CCE( $V$ ) with fits to data (polynomial and linear fits for the two lower-fluence and the two higher-fluence results, respectively) included. (b) Measured and simulated (dotted for 600 V, dashed for 800 V and solid curves for 1 kV, with markers on  $n$ -on- $p$  curves) CCE( $\Phi_{\text{eff}}$ ).



(a)



(b)

Figure 7: CCE at highest-fluence region as a function of voltage and fluence for 120  $\mu\text{m}$  nominal thickness sensors at -30  $^{\circ}\text{C}$ . Sensor identification is indicated in the legends, as well as effective fluences (in units of  $\text{n}_{\text{eq}}\text{cm}^{-2}$ ) in panel (a). CCE = 1 corresponds to the MIP-induced charge of 9  $\text{ke}^{-}$  [16]. (a) Measured CCE( $V$ ) with polynomial fits to data. (b) Measured CCE( $\Phi_{\text{eff}}$ ) with corresponding logarithmic and polynomial fits for both dd-FZ sensor polarities.

120- $\mu\text{m}$ -thick sensors close to the fluence of  $10^{16} \text{ n}_{\text{eq}}\text{cm}^{-2}$  are able to collect about 3.6 at 600 V, 5.4 at 800 V, and 7.3  $\text{ke}^-$  at 1 kV of the 9  $\text{ke}^-$  generated in the silicon bulk.

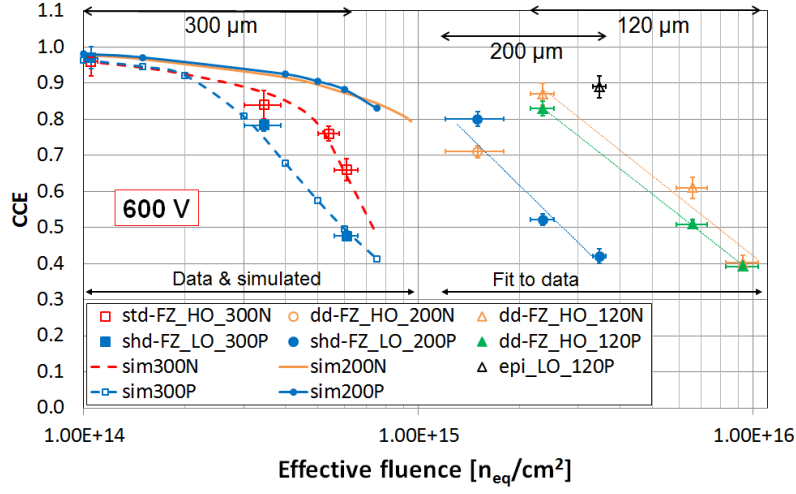
#### 4.2.3. Charge collection of 300P and 200P sensors at extreme fluences

The CCE results of the six *n*-on-*p* samples at neutron fluences up to  $10^{16} \text{ n}_{\text{eq}}\text{cm}^{-2}$  are presented in Figure 11. Both the linear voltage dependence and the absolute values of CCE of the two highest fluence 300P sensors in Figure 11a are closely in line with the results of an earlier charge collection study of 300- $\mu\text{m}$  sensors at extreme neutron fluences [9]. Displayed in Figures 11b and 11c, the fluence evolution of the charge collection in 300P sensors can be estimated by second-order polynomial and logarithmic fits below and above the fluence of  $1.3 \times 10^{15} \text{ n}_{\text{eq}}\text{cm}^{-2}$ , respectively. This agrees with the behavior described in ref. [17] where at higher fluences radiation-induced increase in effective bulk doping generates high enough electric fields to trigger charge multiplication that compensates charge carrier trapping and slows down the degradation of charge collection.

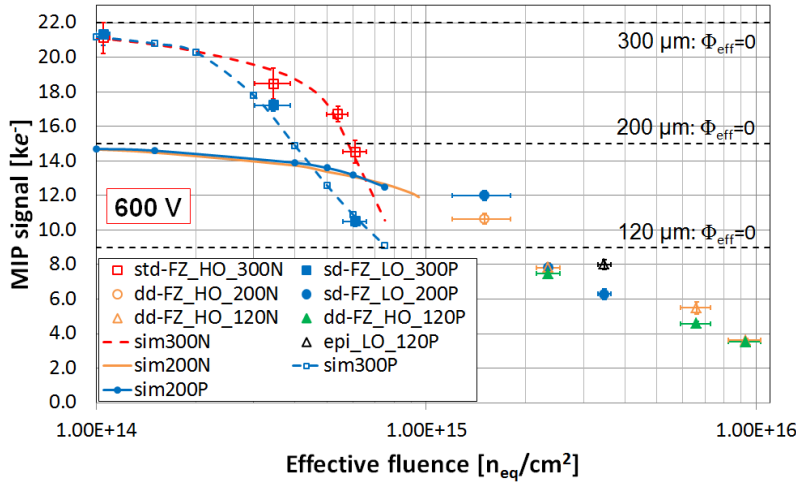
Additionally, the advantageous CCE performance of the 200P sensor in the range  $(1.5\text{--}3.5) \times 10^{15} \text{ n}_{\text{eq}}\text{cm}^{-2}$  (about 20%, 30%, and 36% higher at  $3.5 \times 10^{15} \text{ n}_{\text{eq}}\text{cm}^{-2}$  compared to 300P for 600 V, 800 V, and 1 kV, respectively) diminishes almost completely at the highest fluence in Figure 11b. This is also observed throughout the voltage range of Figure 11a. Similar convergence between sensor thicknesses around  $1 \times 10^{16} \text{ n}_{\text{eq}}\text{cm}^{-2}$  was reported in an earlier study [18]. The highest fluence CCE and  $Q_{\text{coll}}$  values in Figures 11b and 11c are presented in Table 6. The results display some differences in  $Q_{\text{coll}}$  between sensors with high (HO) and low (LO) bulk oxygen content. To investigate further the similar CCE performance of the 200P and 300P sensors at highest neutron fluence, the following relations were considered. The CCE of an irradiated sensor is formulated as a product of two terms, geometrical factor (CCE<sub>GF</sub>) and trapping factor (CCE<sub>t</sub>) [19, 20]

$$\text{CCE} = \text{CCE}_{\text{GF}} \times \text{CCE}_t = \frac{W}{d} \frac{\tau_t}{t_{\text{dr}}} (1 - e^{-\frac{t_{\text{dr}}}{\tau_t}}), \quad (2)$$

where  $W$  is the depletion depth,  $d$  the active thickness of the sensor,  $\tau_t$  the trapping time constant for electrons or holes, and  $t_{\text{dr}}$  the carrier drift time in the depletion region. To solve for  $W$  from the CCE data would first require to determine  $\tau_t$ . This would demand a short-range charge injection (e.g. red laser), where only one type of charge carriers generate the transient signal. However, when it is considered that the investigated samples were exposed to equal fluence (leading to identical  $\tau_t$ ), the CCE results were acquired at equal bias voltage  $V$ , and that the observed carrier drift times were close to equal (mean  $t_{\text{dr}}$  of the 200P and the two

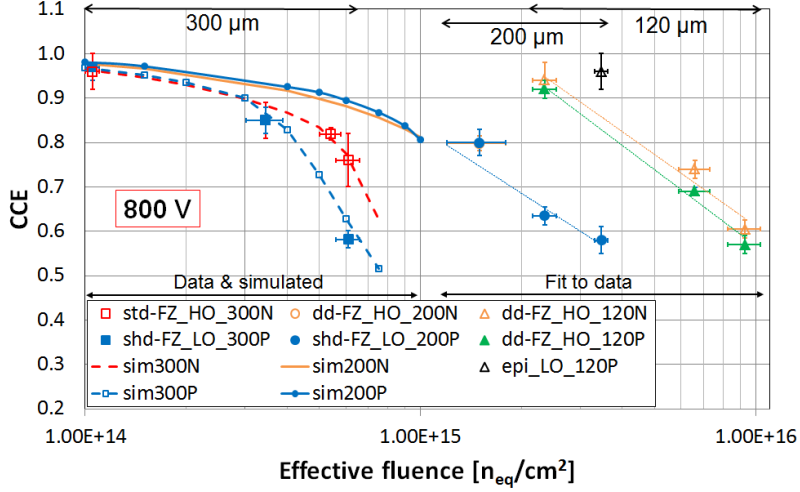


(a)

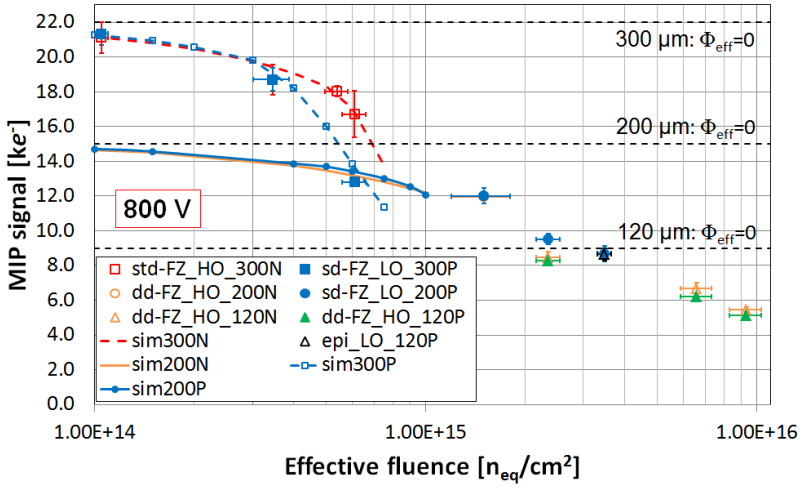


(b)

Figure 8: CCE and MIP charge collection as a function of fluence for the three sensor thicknesses at 600 V and -30 °C temperature, and for the full fluence range [2]. Sensor identification is indicated in the legends. (a) Measured and simulated CCE( $\Phi_{\text{eff}}$ ) with the fluence range of the data points for each sensor thickness indicated. Also indicated, the curves below and above  $1 \times 10^{15} \text{ n}_{\text{eq}}\text{cm}^{-2}$  are simulated results (thick solid and dashed) and logarithmic fits to data (thin dotted), respectively. (b) Measured and simulated  $Q_{\text{coll}}(\Phi_{\text{eff}})$  from MIP charge deposition. The black dashed lines indicate the  $Q_{\text{coll}}$  for each active thickness at CCE = 1 [16].



(a)



(b)

Figure 9: Corresponding CCE and MIP charge collection as a function of fluence to Figure 8 at 800 V. Sensor identification is indicated in the legends. (a) Measured and simulated CCE( $\Phi_{\text{eff}}$ ) with the fluence range of the data points for each sensor thickness indicated. Also indicated, the curves below and above  $1 \times 10^{15} \text{ n}_{\text{eq}}\text{cm}^{-2}$  are simulated results (thick solid and dashed) and logarithmic fits to data (thin dotted), respectively. (b) Measured and simulated  $Q_{\text{coll}}(\Phi_{\text{eff}})$  from MIP charge deposition with  $Q_{\text{coll}}$  for each active thickness at CCE = 1 indicated [16].

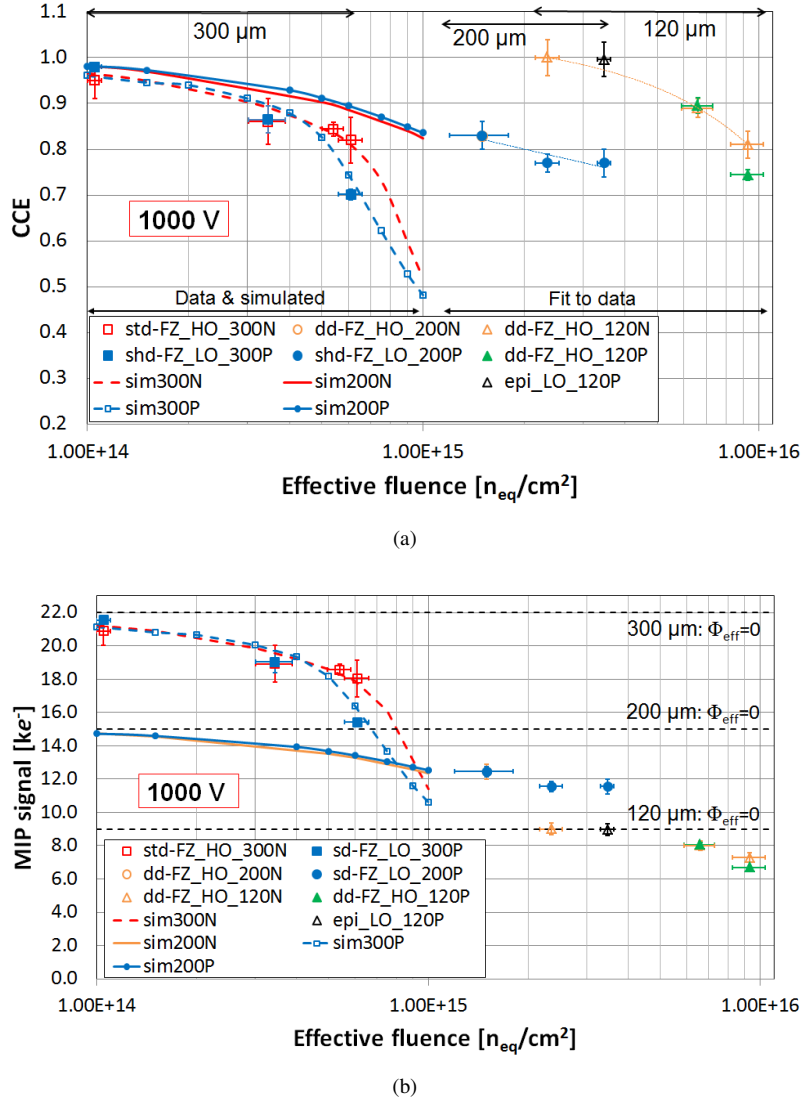


Figure 10: Corresponding CCE and MIP charge collection as a function of fluence to Figures 8 and 9 at 1 kV. Sensor identification is indicated in the legends. (a) Measured and simulated  $CCE(\Phi_{eff})$  with the fluence range of the data points for each sensor thickness indicated. Also indicated, the curves below and above  $1 \times 10^{15} n_{eq}cm^{-2}$  are simulated results (thick solid and dashed) and logarithmic (200P) and polynomial (120N) fits to data (thin dotted), respectively. (b) Measured and simulated  $Q_{coll}(\Phi_{eff})$  from MIP charge deposition with  $Q_{coll}$  for each active thickness at  $CCE = 1$  indicated [16].

Table 6: CCE and  $Q_{\text{coll}}$  of 200P and 300P sensors in Figures 11b and 11c, respectively, at the fluence of  $(9.3 \pm 1.1) \times 10^{15} \text{ n}_{\text{eq}}\text{cm}^{-2}$  and for 600 and 800 V.

Sensor thickness & type	CCE(600 V)	$Q_{\text{coll}}(600 \text{ V})$ [ke $^-$ ]	CCE(800 V)	$Q_{\text{coll}}(800 \text{ V})$ [ke $^-$ ]
shd-FZ\_LO\_200P	$0.121 \pm 0.003$	$1.82 \pm 0.05$	$0.186 \pm 0.005$	$2.79 \pm 0.08$
shd-FZ\_LO\_300P	$0.099 \pm 0.007$	$2.18 \pm 0.15$	$0.140 \pm 0.005$	$3.08 \pm 0.11$
std-FZ\_HO\_300P	$0.111 \pm 0.006$	$2.44 \pm 0.12$	$0.16 \pm 0.02$	$3.5 \pm 0.4$

300P diodes at the highest fluence in Figure 11b was  $3.7 \pm 0.2$  ns), leads to the relationship

$$\frac{W_{200\text{P}}}{W_{300\text{P}}} = \frac{\text{CCE}(V)_{200\text{P}}}{\text{CCE}(V)_{300\text{P}}} \frac{d_{200\text{P}}}{d_{300\text{P}}}. \quad (3)$$

Figure 12 shows the depletion-depth ratios when the CCE( $V$ ) results from Figure 11a are inserted into Eq. 3. The ratios remain close to constant in the investigated voltage range with the average values  $W_{200\text{P\_LO}}/W_{300\text{P\_LO}} = 0.87 \pm 0.15$  and  $W_{200\text{P\_LO}}/W_{300\text{P\_HO}} = 0.70 \pm 0.12$ . Thus, for low oxygen concentration 200P and 300P sensors the result indicates that the charge is collected from equal depth in both sensors within uncertainty. However, the ratio is significantly smaller between low and high oxygen concentration 200P and 300P sensors, respectively. This could suggest a beneficial influence of the higher oxygen concentration on the build-up of negative space [14, 21] at extreme fluence, leading to longer depletion depth at given voltage. Trapping times have not been observed to be significantly influenced by the oxygen content after hadron irradiation [15]. Thus, Eq. 3 is expected to be also applicable for comparison between LO and HO sensors.

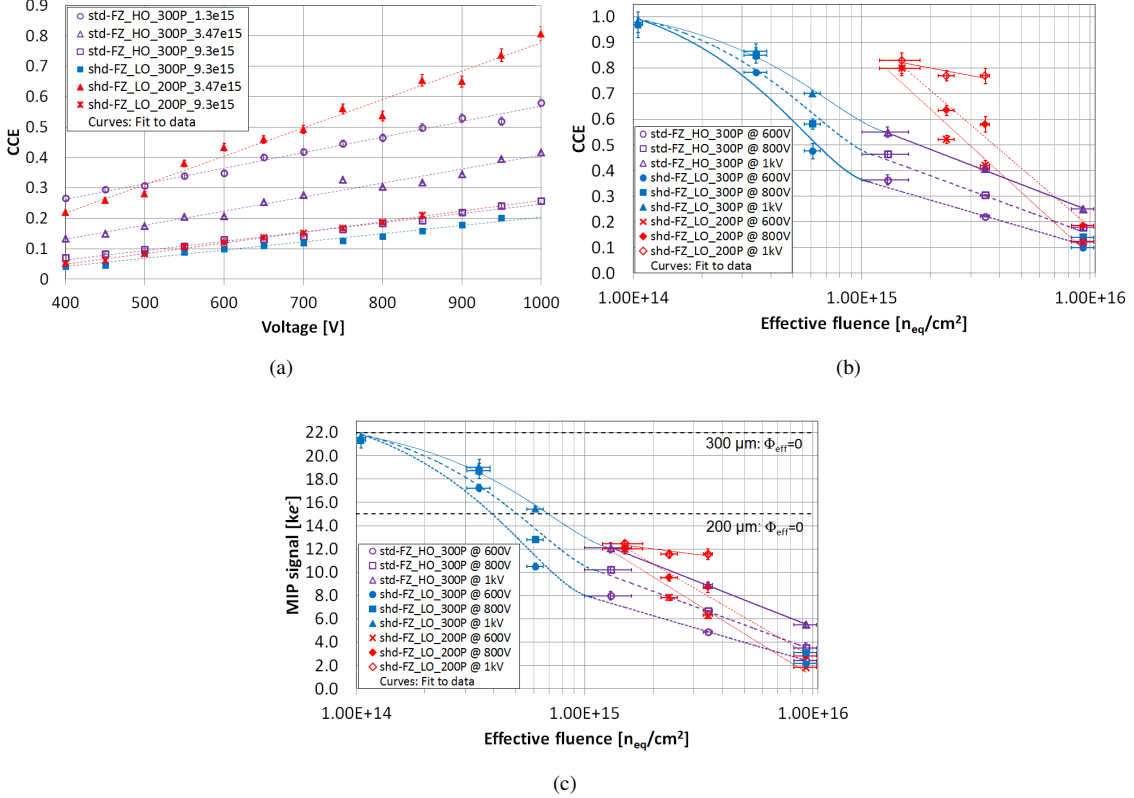


Figure 11: CCE as a function of voltage and fluence, as well as  $Q_{\text{coll}}$  evolution with fluence for 300 and 200- $\mu\text{m}$  thick  $n$ -on- $p$  sensors at  $-30^\circ\text{C}$  in higher-fluence region than anticipated for the two thicknesses at HGCAL. Sensor identification is indicated in the legends, as well as effective fluences (in units of  $\text{n}_{\text{eq}}\text{cm}^{-2}$ ) in panel (a). (a) Measured CCE( $V$ ) with linear fits to data included. (b) Measured CCE( $\Phi_{\text{eff}}$ ) including all measured data points for both sensor thicknesses. The fits to 300P data are polynomial and logarithmic below and above the fluence of  $1.3 \times 10^{15} \text{ n}_{\text{eq}}\text{cm}^{-2}$ , respectively. The fits to 200P data are logarithmic. (c) Measured  $Q_{\text{coll}}(\Phi_{\text{eff}})$  from MIP charge deposition with  $Q_{\text{coll}}$  for both active thicknesses at CCE = 1 indicated [16].

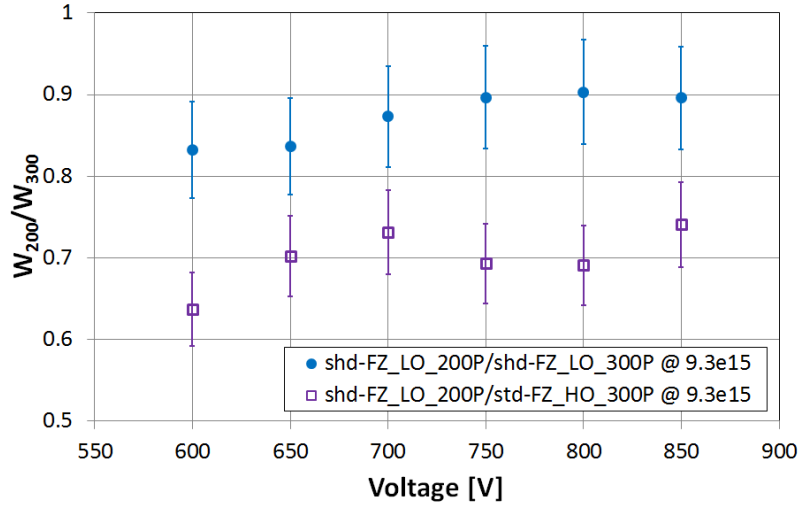


Figure 12: Depletion-depth ratios as a function of voltage for 300- $\mu\text{m}$  (300P) and 200- $\mu\text{m}$  (200P) thick  $n$ -on- $p$  diodes at the highest fluence in Figures 11b and 11c, and calculated by Eq. 3. Sensor identification and effective fluences (in units of  $n_{\text{eq}}\text{cm}^{-2}$ ) are indicated in the legend.

#### 4.3. Full depletion voltages

The fluence evolution of full depletion voltage ( $V_{\text{fd}}$ ) is presented in Figure 13 with measured and simulated results of 300- and 200- $\mu\text{m}$ -thick diodes in Figures 13a and 13b, respectively, and measured results of 120- $\mu\text{m}$ -thick diodes in Figure 13c. The simulated results in the lower-fluence region were produced by applying the neutron defect model using as an input the leakage current extracted  $\Phi_{\text{eff}}$  from Table 4, and frequencies in the range of the measured  $CV$  ( $\mathcal{O}(10^4 \text{ Hz})$ ). The simulated  $V_{\text{fd}}$  was extracted both from  $CV$ -curve and from the voltage where electric field had extended throughout the active thickness of the sensor. The frequency was tuned until the two results were in agreement.

$V_{\text{fd}}$  was defined as the crossing point of the two linear fits made on the dynamic and static regions of the reciprocal capacitance curve, as demonstrated in Figures 14 and 15. Measurements were carried out at frequencies from 20 to 50 kHz, and to take into account the increasing frequency dependence [22, 23] of  $V_{\text{fd}}$  with fluence, the two verifying methods utilized were the aforementioned simulations up to  $1 \times 10^{15} \text{ n}_{\text{eq}}\text{cm}^{-2}$  for both sensor polarities and analytical method using parametrized effective bulk doping for  $n$ -on- $p$  sensors [17, 24]. To reach analytical  $V_{\text{fd}}(\Phi_{\text{eff}})$ , the fluence evolution of effective bulk doping was considered as

$$N_A(\Phi_{\text{eff}}) = g_{\text{eff}}\Phi_{\text{eff}} + N_A(0)e^{-c\Phi_{\text{eff}}}, \quad (4)$$

where  $g_{\text{eff}}$  is the acceptor creation coefficient with a standard value of  $0.02 \text{ cm}^{-1}$  and saturated value of  $0.01 \text{ cm}^{-1}$  at high fluences [17, 25].  $N_A(0)$  and  $N_A(\Phi_{\text{eff}})$  are the acceptor concentrations before and after irradiation, respectively, and  $c = 3 \times 10^{-14} \text{ cm}^2$  [24] is a constant that depends on the initial acceptor concentration and on the type of irradiation.  $V_{\text{fd}}(\Phi_{\text{eff}})$  is then given by the relation [12]

$$V_{\text{fd}}(\Phi_{\text{eff}}) = \frac{ed^2}{2\epsilon_s} N_A(\Phi_{\text{eff}}), \quad (5)$$

where  $e$  is the elemental charge,  $d$  the active thickness of the sensor and  $\epsilon_s$  the permittivity of silicon. Values for  $N_A(0)$  in Figures 13b and 13c were  $4.03 \times 10^{12} \text{ cm}^{-3}$  for shd-FZ 200P-sensors, and  $4.19 \times 10^{12}$  and  $2.1 \times 10^{12} \text{ cm}^{-3}$  for dd-FZ 120P- and epitaxial 120P-sensors, respectively.

Since full depletion can be monitored in the simulation by the extension of the electric field throughout the active thickness of the sensor, it can be used to verify measured  $V_{\text{fd}}$ -values. Displayed in Figure 13a, the simulation is within uncertainties of all data points and exhibits linear increase with fluence.

When analytical  $V_{\text{fd}}(\Phi_{\text{eff}})$  with standard  $g_{\text{eff}}$  is compared to the simulated and measured values of 200P-sensors in Figure 13b, the results are in close agreement up to the fluence of  $1.5 \times 10^{15} \text{ n}_{\text{eq}}\text{cm}^{-2}$ . The corresponding comparison for 120P-sensors in Figure 13c shows agreement up to the fluence of about  $3.5 \times 10^{15} \text{ n}_{\text{eq}}\text{cm}^{-2}$ . In addition, when the measured  $V_{\text{fd}}$  is estimated to be about 1.5 kV for the 300P sensor at the lowest fluence of  $(1.3 \pm 0.3) \times 10^{15} \text{ n}_{\text{eq}}\text{cm}^{-2}$  in Figure 14d, this is reproduced by the analytical  $V_{\text{fd}}(\Phi_{\text{eff}})$  at the fluence of  $1.1 \times 10^{15} \text{ n}_{\text{eq}}\text{cm}^{-2}$ . Beyond these fluences the measured  $V_{\text{fd}}$  results display less steep increase with fluence than the analytical model with standard  $g_{\text{eff}}$ . However, analytical  $V_{\text{fd}}(\Phi_{\text{eff}})$  with intermediate ( $0.013 \text{ cm}^{-1}$ ) and saturated  $g_{\text{eff}}$ -values reproduces closely the data points at second highest and highest fluences in Figure 13c, respectively. Additionally, the fluence evolution of  $V_{\text{fd}}$  above  $1 \times 10^{15} \text{ n}_{\text{eq}}\text{cm}^{-2}$  in Figure 13c is logarithmic, with a fit value of  $(0.33 \pm 0.11) \ln(x) - (11 \pm 4)$ , as opposed to the linear behavior below  $1 \times 10^{15} \text{ n}_{\text{eq}}\text{cm}^{-2}$  seen in Figure 13a. These observations support the saturating behavior of the acceptor creation mechanism at high fluences, as described in ref. [17].

Also visible in Figure 13a is the effect of SCSI, discussed in Section 4.2.2, in the  $n$ -type doped silicon substrate, which results in the decrease of  $V_{\text{fd}}(300\text{N})$  from 200 V before irradiation to about 40 V at about  $1 \times 10^{14} \text{ n}_{\text{eq}}\text{cm}^{-2}$ . Thus, the combined information from measured and simulated data suggests that 300N sensors operated at 600 V are fully depleted below the fluence of  $5 \times 10^{14} \text{ n}_{\text{eq}}\text{cm}^{-2}$ , while the corresponding fluence limit for 300P sensors is below  $3 \times 10^{14} \text{ n}_{\text{eq}}\text{cm}^{-2}$ . Furthermore, the results indicate that operating at 800 V extends the fluence region where the 300P sensor is still fully depleted at about  $4 \times 10^{14} \text{ n}_{\text{eq}}\text{cm}^{-2}$ .

Figure 13b shows that both polarities of 200- $\mu\text{m}$ -thick sensors are fully depleted at 800 V below a fluence

of about  $1.5 \times 10^{15} \text{ n}_{\text{eq}}\text{cm}^{-2}$  and below about  $1 \times 10^{15} \text{ n}_{\text{eq}}\text{cm}^{-2}$  at 600 V. At about  $3.5 \times 10^{15} \text{ n}_{\text{eq}}\text{cm}^{-2}$ , the 120P epitaxial diode is still reaching full depletion at 600 V in Figure 13c.

## 5. Discussion

1. The 300N std-FZ(HO) sensor displays better CCE performance to 300P shd-FZ(LO) for a given operating voltage above about  $4 \times 10^{14} \text{ n}_{\text{eq}}\text{cm}^{-2}$  due to SCSI, which enables it to be fully depleted at significantly lower voltages than the 300P sensor (the 300N sensor is fully depleted at 600 V up to the fluence of about  $5 \times 10^{14} \text{ n}_{\text{eq}}\text{cm}^{-2}$ , while the 300P sensor is not fully depleted at 800 V above the fluence of about  $4 \times 10^{14} \text{ n}_{\text{eq}}\text{cm}^{-2}$ ). At the fluence of about  $6 \times 10^{14} \text{ n}_{\text{eq}}\text{cm}^{-2}$   $\Delta\text{CCE}$  of  $(17 \pm 2)\%$  in favor of the 300N sensor is observed at 600 and 800 V, and 12% at 1 kV. Similar CCE behavior was observed in the earlier studies [2, 5].
2. No clear difference was observed in the CCE performance of 120- $\mu\text{m}$ -thick dd-FZ(HO) diodes between the sensor polarities at the highest fluence, which is also in agreement with the earlier observations [2, 5]. One of the main advantages of the *n*-on-*p* sensor at fluences above  $1 \times 10^{15} \text{ n}_{\text{eq}}\text{cm}^{-2}$  is the superposition of the weighting field and the electric field maxima on the segmented side of the planar sensor, while in the *p*-on-*n* sensor after SCSI, these are located on the opposite sides of a planar sensor. In strip and pixel sensors used in tracking and vertexing detectors, the effect of the weighting field is optimized by sensor geometry, which favors electron contribution to the signal collected at the  $\text{n}^+$  electrode [9, 26], while in the large area pad detectors, the benefit from the weighting field (simply the inverse of the sensor thickness  $1/d$  [27]) is minimal, leading to negligible differences in CCE performances between sensor types at high fluences.
3. The slowing down of the degradation of charge collection of 300P-sensors at fluences above  $1 \times 10^{15} \text{ n}_{\text{eq}}\text{cm}^{-2}$  in Figures 11b and 11c can be interpreted as a result of charge multiplication (CM) that compensates charge carrier trapping [17]. Since CM is a function of electric field, its effect is expected to be more pronounced in thinner sensors that have higher electric fields for a given bias voltage during charge collection. Thus, higher influence of CM could explain the previously reported [5] better charge collection performance of epitaxial 100- $\mu\text{m}$  active thickness diodes relative to the 120- $\mu\text{m}$  dd-FZ diodes at the fluence of  $1.0 \times 10^{16} \text{ n}_{\text{eq}}\text{cm}^{-2}$ .
4. TCAD simulation tuning with input from *CV/IV*-measurements before irradiation and IR-TCT parameters resulted in closely reproduced transient signal shapes that minimize error sources for modeling of radiation damage in silicon. Further study will need to be conducted to develop a neutron defect

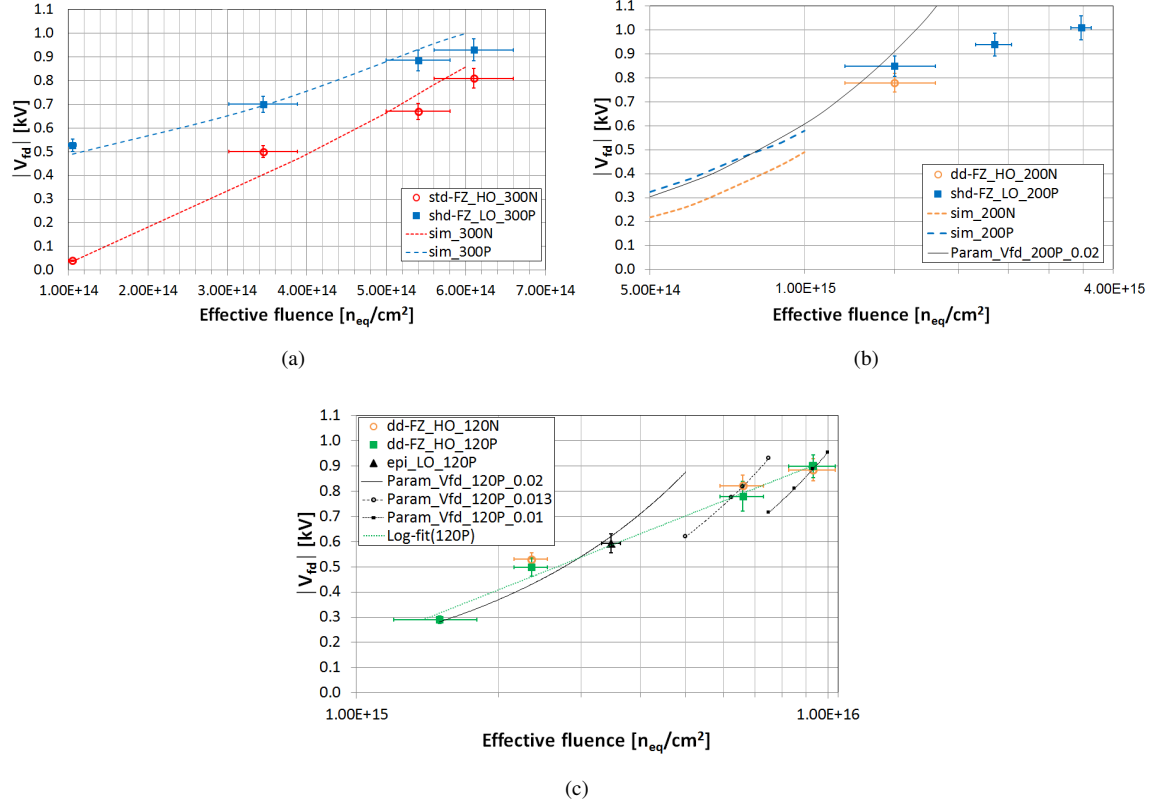


Figure 13: Evolution of full depletion voltage as a function of  $\Phi_{\text{eff}}$  for the fluence ranges anticipated for the three sensor thicknesses at HGCAL. Simulations are applied up to the neutron defect model's validated fluence limit [7]. The corresponding  $CV$ -curves are presented in Figures 14 and 15. (a) Measured (markers) and simulated (dashed curves)  $V_{fd}(\Phi_{\text{eff}})$  for 300- $\mu\text{m}$  thick sensors. Initial  $V_{fd}$  before irradiation for 300N and 300P were 200 V and 300 V, respectively. (b) Measured and simulated  $V_{fd}(\Phi_{\text{eff}})$  for 200- $\mu\text{m}$  thick sensors.  $V_{fd}$  before irradiation for 200N and 200P were 95 V and 130 V, respectively. Parametrized  $V_{fd}(\Phi_{\text{eff}})$  was calculated using Eq. 5 with standard value of  $g_{\text{eff}} = 0.02 \text{ cm}^{-1}$  [17]. (c) Measured  $V_{fd}(\Phi_{\text{eff}})$  for 120- $\mu\text{m}$  thick sensors.  $V_{fd}$  before irradiation for both 120N and 120P was 50 V, while for epitaxial 120P it was 20 V. Parametrized  $V_{fd}(\Phi_{\text{eff}})$  was calculated using Eq. 5 with standard ( $0.02 \text{ cm}^{-1}$ ), intermediate ( $0.013 \text{ cm}^{-1}$ ) and saturated ( $0.01 \text{ cm}^{-1}$  [17]) values of  $g_{\text{eff}}$ . The logarithmic fit value for 120P sensors is  $(0.33 \pm 0.11) \ln(x) - (11 \pm 4)$ .

model that is able to reproduce all properties of irradiated silicon sensors observed in this and previous studies in the fluence range of  $(0.1 - 1) \times 10^{16} \text{ n}_{\text{eq}}\text{cm}^{-2}$ .

## 6. Summary

After neutron irradiation campaigns at RINSC and MNRC, the electrical characterization of 12 and 18 irradiated samples diced from 8-inch and 6-inch wafers, respectively, was completed and the most probable effective fluences were extracted from the leakage currents above  $V_{\text{fd}}$ . The results of the CCE study of test diodes at -30 °C and for operating voltages of 600, 800, and 1000 V, along with the results of the electrical properties, indicate the following:

- For 300-μm-thick sensors:
  - TCAD simulation verifies and complements the CCE results from the IR-TCT measurements.
  - CCEs of both sensor polarities gain about 10% due to increased operating voltage from 600 V to 800 V at highest expected fluences, resulting in CCEs of about 76% and 60% for the 300N and 300P sensors, respectively. Corresponding gains at 1 kV are 16% and 22%, respectively. At the lowest lifetime fluence, a CCE of about 96% was observed for both sensor types. The 300N sensor displays better CCE performance compared to the 300P above the fluence of about  $4 \times 10^{14} \text{ n}_{\text{eq}}\text{cm}^{-2}$  due to SCSI.
  - In the fluence range  $1 \times 10^{14} - 1 \times 10^{16} \text{ n}_{\text{eq}}\text{cm}^{-2}$  evidence of CM, that slows down the degradation of charge collection performance by compensating charge carrier trapping, was observed at fluences above  $1 \times 10^{15} \text{ n}_{\text{eq}}\text{cm}^{-2}$ .
- For 200-μm-thick sensors:
  - The CCE of the 200P increases by about 11% and 25% from operating at 800 V and 1 kV, respectively, instead of 600 V, at the fluence of about  $2.5 \times 10^{15} \text{ n}_{\text{eq}}\text{cm}^{-2}$ , resulting in CCEs of about 63% and 77%, respectively. At the lowest fluence, a CCE of about 91% is expected from simulation for both sensor types. Furthermore, the CCE performance of 200P sensor displays 16% and 35% improvement from increasing the operating voltage from 600 V to 800 V and 1 kV, respectively, at the fluence of about  $3.5 \times 10^{15} \text{ n}_{\text{eq}}\text{cm}^{-2}$ , resulting in CCEs of about 60% and 77%, respectively.

- Combined measured, simulated and analytically calculated  $V_{fd}$  results suggest that the 200P-sensor is not fully depleted at 800 V beyond the fluence of about  $1.3 \times 10^{15} \text{ n}_{\text{eq}}\text{cm}^{-2}$ , while it can be operated at 600 V fully depleted below the fluence of  $1 \times 10^{15} \text{ n}_{\text{eq}}\text{cm}^{-2}$ .
- For 120- $\mu\text{m}$ -thick sensors:
  - The collected charges from a MIP-induced charge deposition close to the fluence of  $10^{16} \text{ n}_{\text{eq}}\text{cm}^{-2}$  show values of 0.58 at 600 V, 0.87 at 800 V, and 1.17 fC at 1 kV operating voltage. Thus, the sensors require more than 800 V biasing to collect at least 1 fC from a single-MIP-charge-injection at highest lifetime fluences.
  - The CCE performance of both polarity sensors improves by 20% and 40% due to increasing the operating from 600 V to 800 V and 1 kV, respectively, at the fluence of about  $9.3 \times 10^{15} \text{ n}_{\text{eq}}\text{cm}^{-2}$ . At lowest investigated fluences, both sensor types display essentially non-degraded CCE performance.
  - Similar CCE performance was observed between sensor types at the highest fluence due to minimal benefit from the weighting field to electron collection in *n*-on-*p* pad sensors.
  - Combined measured and analytically calculated  $V_{fd}$  results suggest that 120P-sensors are not fully depleted at 800 V above the fluence of about  $6 \times 10^{15} \text{ n}_{\text{eq}}\text{cm}^{-2}$ , while both polarity sensors are fully depleted at 600 V below the lifetime fluence of about  $3.5 \times 10^{15} \text{ n}_{\text{eq}}\text{cm}^{-2}$ . Fluence evolution of  $V_{fd}$  above  $1 \times 10^{15} \text{ n}_{\text{eq}}\text{cm}^{-2}$  is logarithmic and shows evidence of the saturation of acceptor creation mechanism above  $5 \times 10^{15} \text{ n}_{\text{eq}}\text{cm}^{-2}$ .
- CCE analysis suggests that the similar charge collection performance between 200P(LO) and 300P(LO) sensors at the fluence of about  $(9.3 \pm 1.1) \times 10^{15} \text{ n}_{\text{eq}}\text{cm}^{-2}$  results from close-to-equal depletion regions. Higher  $Q_{\text{coll}}$  in 300P(HO) relative to 200P/300P(LO) at equal fluence could be evidence of small benefit to radiation hardness from higher oxygen content in the sensor bulk at extreme neutron fluences.

## Acknowledgements

Access and operation of the RINSC and MNRC reactors were coordinated by U. Heintz and N. Hinton of Brown University and by M. Tripathi and W. D. Frey of UC-Davis, respectively. We thank K. Zinsmeyer, P. Cruzan and C. Perez of TTU for their expert technical support, as well as J. Christian and P. Wibert for their contributions to the sensor characterization measurements.

## References

- [1] F. Gianotti, et al., Physics potential and experimental challenges of the LHC luminosity upgrade, *Eur. Phys. J. C* 39 (2005) 293–333. doi:10.1140/epjc/s2004-02061-6.
- [2] CMS Collaboration, The Phase-2 Upgrade of the CMS Endcap Calorimeter, CERN-LHCC-2017-023, Tech. rep., CERN, Geneva, CMS-TDR-019, technical Design Report of the endcap calorimeter for the Phase-2 upgrade of the CMS experiment, in view of the HL-LHC run (Nov. 2017). URL <https://cds.cern.ch/record/2293646>
- [3] E. Fretwurst, et al., Radiation damage studies on MCz and standard and oxygen enriched epitaxial silicon devices, *Nucl. Instr. & Meth. A* 583 (2007) 58–63. doi:10.1016/j.nima.2007.08.194.
- [4] A. Affolder, et al., Silicon detectors for the sLHC, *Nucl. Instr. & Meth. A* 658 (2011) 11–16. doi:10.1016/j.nima.2011.04.045.
- [5] E. Currás, et al., Radiation hardness study of Silicon Detectors for the CMS High Granularity Calorimeter (HGCAL), *JINST* 12 (2017) C02056. doi:10.1088/1748-0221/12/02/C02056.
- [6] T. Peltola, Experimental and simulation study of irradiated silicon pad detectors for the CMS High Granularity Calorimeter, in: 2017 IEEE Nuclear Science Symposium and Medical Imaging Conference (NSS/MIC), IEEE, Atlanta, GA, USA, 2017. doi:10.1109/NSSMIC.2017.8532957.
- [7] R. Eber, Investigations of new sensor designs and development of an effective radiation damage model for the simulation of highly irradiated silicon particle detectors, Ph.D. thesis, Karlsruhe Institute of Technology (2013). URL <http://ekp-invenio.physik.uni-karlsruhe.de/record/48328/files/EKP-2014-00012.pdf>
- [8] T. Peltola, Simulation of radiation-induced defects, *PoS* 031 (2015) (VERTEX2015). doi:<https://doi.org/10.22323/1.254.0031>.
- [9] G. Kramberger, V. Cindro, I. Mandić, M. Mikuž, M. Zavrtanik, Charge collection studies on custom silicon detectors irradiated up to  $1.6 \cdot 10^{17} n_{eq}/cm^2$ , *JINST* 8 (2013) P08004. doi:10.1088/1748-0221/8/08/P08004.

[10] M. S. Lazo and D. M. Woodall and P. J. McDaniel, Silicon and silicon dioxide neutron damage functions, Tech. rep., Sandia National Laboratories, In Proc. Fast Burt React. Workshop, 1986 (1987).  
 URL [https://inis.iaea.org/search/search.aspx?orig\\_q=RN:22038475](https://inis.iaea.org/search/search.aspx?orig_q=RN:22038475)

[11] D. Passeri, F. Moscatelli, A. Morozzi, G. M. Bilei, Modeling of radiation damage effects in silicon detectors at high fluences HL-LHC with Sentaurus TCAD, *Nucl. Instr. & Meth. A* 824 (2016) 443–445. doi:10.1016/j.nima.2015.08.039.

[12] S. M. Sze, *Physics of Semiconductor Devices*, 2nd Edition, John Wiley & Sons, New Jersey, 1981.

[13] M. Moll, Radiation damage in silicon particle detectors –microscopic defects and macroscopic properties–, Ph.D. thesis, University of Hamburg (1999).  
 URL <https://mmoll.web.cern.ch/mmoll/thesis/pdf/moll-thesis.pdf>

[14] G. Lindström, Radiation damage in silicon detectors, *Nucl. Instr. & Meth. A* 512 (2003) 30–43. doi:10.1016/S0168-9002(03)01874-6.

[15] M. Moll, E. Fretwurst, G. Lindström, Leakage current of hadron irradiated silicon detectors – material dependence, *Nucl. Instr. & Meth. A* 426 (1999) 87–93. doi:10.1016/S0168-9002(98)01475-2.

[16] C. Patrignani, et al. (Particle Data Group), Review of particle physics, *Chin. Phys. C* 40 (2016) 100001. doi:10.1088/1674-1137/40/10/100001.

[17] N. Cartiglia, H. Sadrozinski, A. Seiden, Tracking particles at fluences  $5 - 10 \cdot 10^{16} n_{eq}/cm^2$ , *PoS* 029 (2019) (VERTEX2018). doi:10.22323/1.348.0029.

[18] A. Affolder, P. Allport, H. Brown, G. Casse, Effects of Varying Substrate Thickness on the Collected Charge From Highly Irradiated Planar Silicon Detectors, *IEEE Trans. Nucl. Sci.* 58 (6) (2011) 3384–3391. doi:10.1109/TNS.2011.2171058.

[19] CERN RD39 Collaboration, RD39 Status Report 2006, CERN-LHCC-2006-034 (Nov. 2006).  
 URL <http://cds.cern.ch/record/998240/files/lhcc-2006-034.pdf?version=1>

[20] H. W. Kraner, Z. Li, E. Fretwurst, The use of the signal current pulse shape to study the internal electric field profile and trapping effects in neutron damaged silicon detectors, *Nucl. Instr. & Meth. A* 326 (1993) 350–356. doi:10.1016/0168-9002(93)90376-S.

[21] G. Kramberger, V. Cindro, I. Mandić, M. Mikuž, M. Zavrtanik, Effective trapping time of electrons and holes in different silicon materials irradiated with neutrons, protons and pions, *Nucl. Instr. & Meth. A* 481 (2002) 297–305. doi:10.1016/S0168-9002(01)01263-3.

[22] Z. Li, H. W. Kraner, Studies of frequency dependent C-V characteristics of neutron irradiated p<sup>+</sup>-n silicon detectors, *IEEE Trans. Nucl. Sci* 38 (1991) 244–250. doi:10.1109/23.289304.

[23] P. Riedler, Radiation Damage Effects and Performance of Silicon Strip Detectors using LHC Readout Electronics, Ph.D. thesis, University of Vienna (1998).  
 URL <https://cds.cern.ch/record/423114/files/cer-002171220.pdf>

[24] H. Sadrozinski, A. Seiden, N. Cartiglia, 4D tracking with ultra-fast silicon detectors, *Reports on Progress in Physics* 81 (2017) 026101. doi:10.1088/1361-6633/aa94d3.

[25] J. P. Balbuena and others, RD50 Status Report 2008 - Radiation hard semiconductor devices for very high luminosity colliders, CERN-LHCC-SR-003 (Jan. 2009).  
 URL <https://cds.cern.ch/record/1291631/files/LHCC-SR-003.pdf>

[26] G. Kramberger, V. Cindro, I. Mandić, M. Mikuž, M. Zavrtanik, Influence of trapping on silicon microstrip detector design and performance, *IEEE Trans. Nucl. Sci.* 49 (4) (2002) 1717–1723. doi:10.1109/TNS.2002.801517.

[27] S. Ramo, Currents induced by electron motion, *Proc. I.R.E.* 27 (1939) 584–585. doi:10.1109/JRPROC.1939.228757.

## A. Appendix: *CV*-results

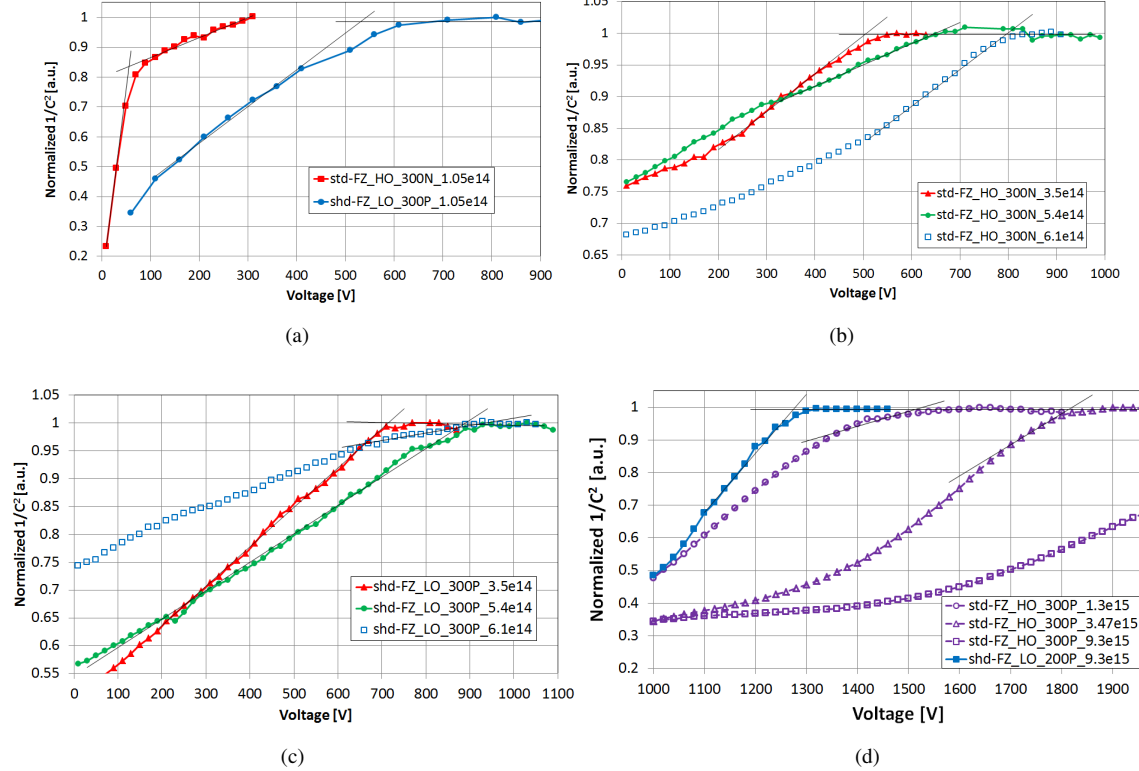


Figure 14: Measured reciprocal capacitances as a function of voltage and extracted  $V_{fd}$ -values (crossing point of two linear fits) for (a) 300N/P sensors at  $(1.05 \pm 0.05) \times 10^{14} \text{ neq cm}^{-2}$ , (b) 300N sensors and (c) 300P sensors corresponding to Figure 13a. Also shown in (d) are the results for 300- $\mu\text{m}$  (300P) and 200- $\mu\text{m}$  (200P) thick *n*-on-*p* diodes irradiated up to about  $10^{16} \text{ neq cm}^{-2}$ . Sensor identification and effective fluences (in units of  $\text{neq cm}^{-2}$ ) are indicated in the legends.

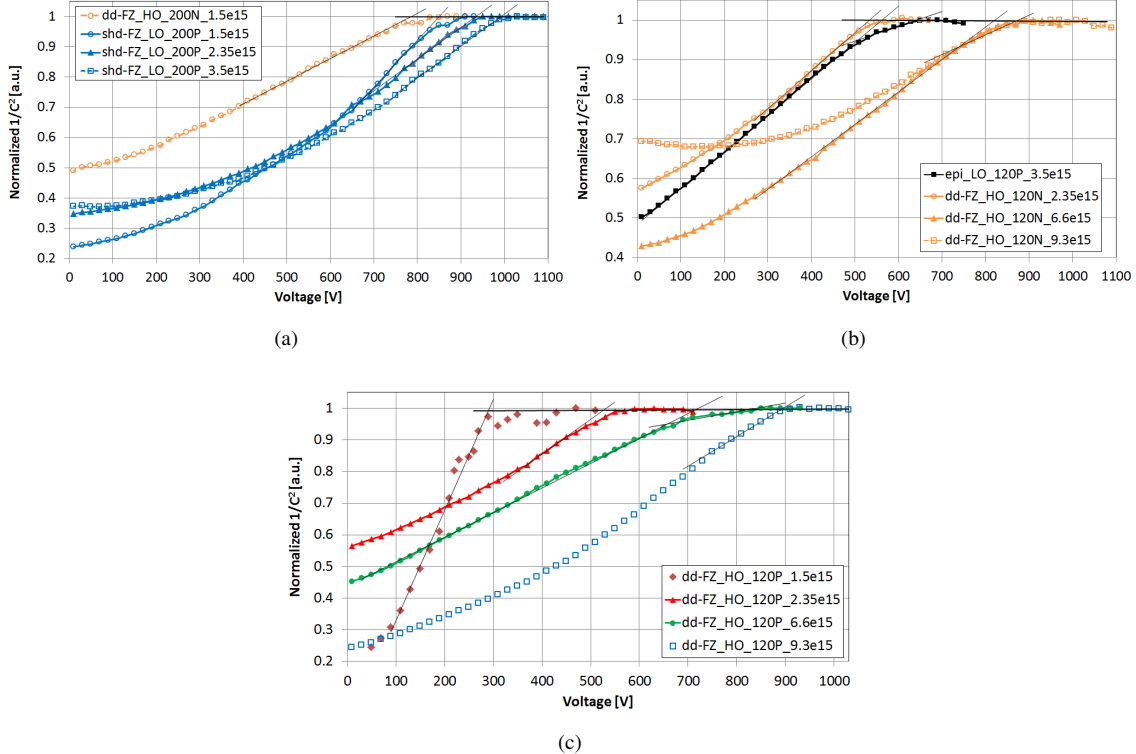


Figure 15: Measured reciprocal capacitances as a function of voltage and extracted  $V_{fd}$ -values (crossing point of two linear fits) for (a) 200N/P sensors, (b) epitaxial 120P and 120N sensors, and (c) 120P sensors corresponding to Figures 13b and 13c, respectively. Sensor identification and effective fluences (in units of  $n_{eq}cm^{-2}$ ) are indicated in the legends.